applied sciences

MDPI

Article

Analysis of Dynamic Behavior of ParReEx Robot Used in Upper Limb Rehabilitation

Daniela Tarnita [1], Ionut Daniel Geonea [1,*], Doina Pisla [2,*], Giuseppe Carbone [3], Bogdan Gherman [2], Nicoleta Tohanean [4], Paul Tucan [2], Cristian Abrudan [4] and Danut Nicolae Tarnita [5]

1 Faculty of Mechanics, University of Craiova, 200512 Craiova, Romania
2 Research Center for Industrial Robots Simulation and Testing CESTER, Technical University of Cluj-Napoca, 400641 Cluj-Napoca, Romania
3 Department of Mechanical, Energy and Management Engineering DIMEG, University of Calabria, 87036 Cosenza, Italy
4 Department of Neurology, University of Medicine and Pharmacy "Iuliu Hatieganu", 400012 Cluj-Napoca, Romania
5 Emergency Hospital of Dolj County, 200528 Craiova, Romania
* Correspondence: ionut.geonea@edu.ucv.ro (I.D.G.); doina.pisla@mep.utcluj.ro (D.P.)

Abstract: This paper presents a dynamic analysis of the ParReEx multibody mechanism, which has been designed for human wrist joint rehabilitation. The starting point of the research is a virtual prototype of the ParReEx multibody mechanism. This model is used to simulate the dynamics of the multibody mechanism using ADAMS in three simulation scenarios: (a) rigid kinematic elements without friction in joints, (b) rigid kinematic elements with friction in joints, and (c) kinematic elements as deformable solids with friction in joints. In all three cases, the robot is used by a virtual patient in the form of a mannequin. Results such as the connecting forces in the kinematic joints and the torques necessary to operate the ParReEx robot modules are obtained by dynamic simulation in MSC.ADAMS. The torques obtained by numerical simulation are compared with those obtained experimentally. Finite element structural optimization (FEA) of the flexion/extension multibody mechanism module is performed. The results demonstrate the operational safety of the ParReEx multibody mechanism, which is structurally capable of supporting the external loads to which it is subjected.

Keywords: dynamic simulation; spherical parallel robot; joint friction; flexible links; rehabilitation; wrist joint

Citation: Tarnita, D.; Geonea, I.D.; Pisla, D.; Carbone, G.; Gherman, B.; Tohanean, N.; Tucan, P.; Abrudan, C.; Tarnita, D.N. Analysis of Dynamic Behavior of ParReEx Robot Used in Upper Limb Rehabilitation. *Appl. Sci.* **2022**, *12*, 7907. https://doi.org/10.3390/app12157907

Academic Editors: Alessandro Gasparetto and Dimitris Mourtzis

Received: 22 June 2022
Accepted: 3 August 2022
Published: 7 August 2022

1. Introduction

Although there has been an increasing emphasis on prevention in recent decades, strokes are one of the leading causes of permanent disability worldwide [1]. In recent decades, strokes have led to the disability and even death of a very large number of people; in recent years, the number of people affected annually is about 13 million [2].

Globally, the leading causes of death are ischemic heart disease, with an incidence of 14.8%, and stroke, with an incidence of 11.8% [3].

Recent studies show that the number of stroke cases is increasing. Taking into account the aging of the population worldwide, there are advanced fears regarding the increasingly limited capacity of European and global medical systems to meet patient care requirements [4]. It is estimated that in the near future, strokes will affect an upper limb in over 85% of cases [5], and the success rate for arm rehabilitation will be only 10% [6] due to the complexity of upper limb movement [7]. In less than 10 years, the annual medical cost per stroke will increase rapidly; for example, in the USA, it will be 2.5 times higher than it was in 2012 [8]. Currently, in developed countries, 3–4% of medical costs are allocated to strokes [9]. Physical rehabilitation is becoming less and less effective as each patient has

to work with a physical therapist [10], but the use of robotic exoskeletons allows for more effective therapy through repetitive movements and adaptive training [11,12].

The use of rehabilitation technology and robotics optimizes the results, minimizes costs by conserving labour and maximizing progressive repetitions, and improves the outcome compared to the high costs of conventional therapy performed as one-on-one training with a professional therapist [13–15].

Numerous articles have been dedicated to the study of robotic structures used for upper limb rehabilitation. Robotic systems for upper limb rehabilitation are the subject of much research. Thus, the design and performance evaluation of the RUPERT exoskeleton for upper limbs is presented in [16]. An innovative robotic system with a spherical architecture is developed and presented in [17]. A parallel robotic system based on a spherical architecture, ASPIRE, was designed for three degrees-of-freedom (DOFs) shoulder rehabilitation, as described in this study. In [18], a study of torque monitoring is performed for the ASPIRE robotic system. Clinical trials based on the use of ASPIRE on post-stroke patients are presented. Further, design optimization is studied based on therapist feedback following clinical evaluation. A study of the ASPIRE robot for upper limb rehabilitation is presented in [19], where, with the help of ADAMS software, the dynamic analysis of the robotic system is performed. The study of hand joint movements is also presented in [20]. Classifications and analyses of these structures can be found in [21].

Over the past decade, many robotic devices have been designed to enhance the motor rehabilitation process. In [22–25], the authors noted an improvement in quality of life and concluded that robot-assisted therapy is beneficial for recovering the motor functions of the upper limbs in patients with early-stage stroke. Neurorehabilitation therapy including task-oriented training with the ARMin exoskeleton robot can enhance improvement of motor function in a chronically impaired paretic arm after stroke more effectively than conventional therapy [23].

A hybrid exoskeleton named EFW Exo II is developed for the motor function rehabilitation of elbow, forearm and wrist, and the ranges of motion meet the rehabilitation demands of daily living [24]. For clinical trials, an acquisition data system based on wearable sensors was used; due to their advantages, these systems are often used in evaluating biomechanical human data [25–31].

Several robotic devices have been developed to rehabilitate the wrist joint, which, after the shoulder, is the second-most complex joint of the human upper limb. The authors of [32] review the main wrist rehabilitation robots developed recently in terms of mechanical design and aspects of control, and highlight aspects of experimental tests of these robots on patients with neurological disorders.

Krebs et al. studied a wrist rehabilitation robot that offers three DOFs [33], which, mounted on the accompanying robot, MIT-MANUS [34,35], has become a very suitable tool for the rehabilitation of the shoulders and elbow. Another wrist robot [36] with three active DOFs was developed with a similar structure and an additional passive prismatic joint. RiceWrist [37], as an electrically operated forearm–wrist exoskeleton, uses a serial RRR manipulator and cable transmissions to rehabilitate the wrist and radio–ulnar joints. Robots presented in [38,39] allow the rehabilitation of two movements: forearm supination/pronation and wrist flexion/extension, while in [40], the human wrist has been simplified to a single DOF—namely flexion/extension. A parallel wrist rehabilitation robot driven by two pneumatic actuators is developed in [41] to rehabilitate two DOFs: flexion/extension and radial/ulnar deviation.

Patient safety is a critical milestone in the development of robotic systems for medical applications to avoid any unwanted damage. In this case, it can be achieved by implementing a dynamic model in the control system [42,43] using various principles such as: the Lagrange–Euler formalism, the principle of virtual work [44] or the Newton–Euler equations [45–47].

ADAMS View, software designed for the analysis of mobile systems dynamics, with an increased accuracy of kinematic and dynamic results obtained from numerical simulations

has been used in several studies of robotic systems for rehabilitation of human movements, such as exoskeletons or flexible robotic structures for minimally invasive surgery [19,27,48,49].

For structural optimization of a kinematic element, one of the most powerful software programs is ANSYS. In [19], we presented finite element analysis of a kinematic element in the ASPIRE robot structure.

The aim of this study is to analyze from a kinematic, dynamic and experimental point of view a robotic system designed for the rehabilitation of the human wrist joint of post-stroke survivors. Numerical simulations are performed for the robot mounted on the wrist of a virtual patient. For validation of the dynamic model built in ADAMS, the results obtained by numerical simulation are compared with those obtained experimentally. Three distinct situations will be studied:

- The kinematic elements are considered as rigid bodies, and the friction in the kinematic joints is not considered;
- The kinematic elements are considered as rigid bodies, and the friction in the robot joints is considered;
- The kinematic elements are considered as flexible bodies, and the friction in the robot joints is considered.

The paper is structured as follows: after the introduction, a functional constructive description of the ParReEx robot for wrist rehabilitation is presented. Dynamic analysis is presented in ADAMS for the three considered operating hypotheses. Then, structural optimization is performed for the circular guidance of the ParReEx robot. At the end, experimental results, discussions, and conclusions are presented.

2. Constructive and Functional Description of the ParReEx-Wrist Robot

The ParReEx-wrist robotic system is designed for the rehabilitation of the wrist, namely flexion and extension of the wrist and ulnar and radial deviation of the wrist [49]. The robot has two degrees of freedom (DoF), one for each type of motion (Figure 1), namely: the revolute joint q_1 to perform flexion–extension and the revolute joint q_2 to perform radial–ulnar deviation. Each joint separately actuates a kinematic chain as follows: q_1 actuates an RR chain consisting of the R_1 and R_3 revolute joints connected through link d around the OZ axis; q_2 actuates link *e* around the OY axis, fixed between two bearings. Links d and e are connected via two revolute joints, namely R_2 and R_3, required to perform the circumduction motion (which is a combination of flexion–extension and ulnar–radial deviation motions). Notations used in Figure 1 represents: q_1—flexion–extension motion; q_2—radial–ulnar deviation motion; R_1, R_2, R_3, R_4—revolute joints; e, d—mechanism links.

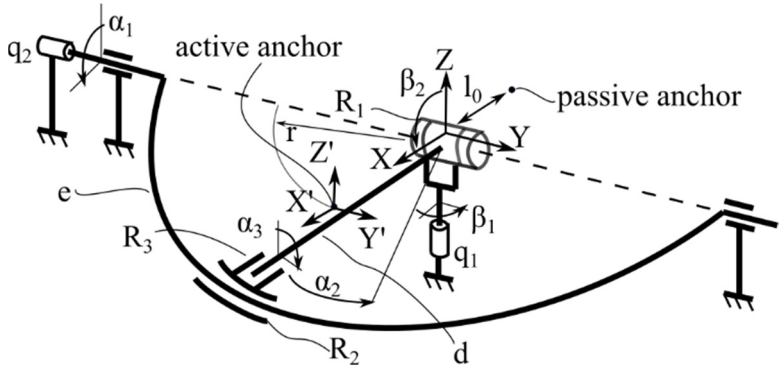

Figure 1. The ParReEx-wrist kinematic scheme [47].

The ParReEx-wrist CAD model is presented in Figure 2. Motor (1) achieves the flexion–extension motion of the wrist through a set of bevel gears (3) and a custom-made circular rail and sledge guiding (4). Motor (2) performs radial–ulnar deviation using a timing belt and pulleys (5). The patient's hand is supported using the wrist support (6), which acts as active anchor, and the forearm support (7), which acts as passive anchor. Since the patient's

wrist is placed above the fixed coordinate system (Figure 1), as the intersection between the flexion–extension and radial–ulnar deviation robot motion axis, an additional straight rail-and-sledge mechanism (8) is required, as well as a spherical joint (9) to perform the circumduction motion.

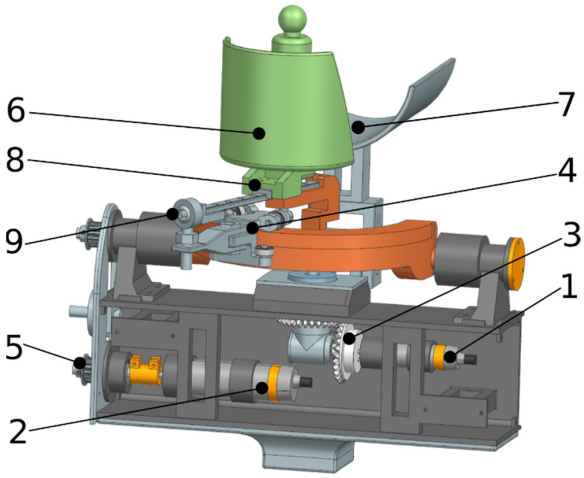

Figure 2. The ParReEx-wrist CAD model.

Notations used in Figure 2 represents: 1—motor for flexion–extension motion; 2—motor for radial–ulnar deviation motion; 3—bevel gears; 4—sledge pulleys; 5—belt transmission; 6—wrist support; 7—forearm support; 8—straight rail and sledge mechanism; 9—spherical joint.

The ParReEx-wrist experimental model is presented in Figure 3. Based on the virtual prototype of the ParReEx robot, the execution drawings for the component parts of the assembly were made. The housing of the robotic system and the component parts, such as those numbered 6, 7 and 8 in Figure 2, are manufactured by additive manufacturing. For this purpose, we used a 3D printer, which works on the fused deposit manufacturing principle. For the execution of the printed parts, we used 3D models, and, using Cura Ultimaker software, we made the G-code for 3D printing. The printer uses ABS (acrylonitrile butadiene styrene) wire, which is melted by the print head, and successive layers are deposited to achieve the shape of the parts. Thus, these parts are assembled to realize the prototype of the robotic system, as shown in Figure 3, where the robotic system is shown in the situation of its use by a patient.

Figure 3. The ParReEx-wrist experimental model.

3. Dynamic Analysis in MSC.ADAMS of ParReEx-Wrist Robot

3.1. Dynamic Analysis in MSC.ADAMS of ParReEx-Wrist Robot, Considering the Kinematic Elements as Rigid Solids without Considering Joint Friction

Based on the structural scheme of the ParReEx robot, a virtual prototype is designed using Unigraphics NX software. The development of the virtual prototype is necessary from two aspects: it will be used to simulate the dynamic behavior of the robot, as well as for structural optimization with the finite element method. The development of the dynamic model in ADAMS involves the following steps:

✓ Definition of the materials of the robot subassemblies.

Robot element materials can be selected from the ADAMS database, or new materials can be defined by their properties. In this case, the materials of the component elements are defined in the database, and their mechanical properties are further explained. For each component element of the robot, we specify the material from which it is made. Thus, in the robot component, we have parts that are made of aluminum alloy with the following properties: density = 2470 kg/m^3, Young's Modulus = 7.17 $\times$ 10^{10} N/m^2 and Poisson's ratio = 0.33. The robot housing, the circular guide and the elements supporting the patient's hand are made of ABS. Acrylonitrile butadiene styrene, commonly known as ABS, is a polymer and opaque thermoplastic comprised of acrylonitrile, butadiene, and styrene. ABS is an incredibly versatile and durable plastic, making it an extremely popular material used in a variety of industries. The mechanical properties of this material are as follows: density = 1.15 $\times$ 10^3 kg/m^3, Young's Modulus=1.6 $\times$ 10^{10} N/m^2 and Poisson's ratio = 0.340.

✓ Kinematic joints related to the robot structure are defined.

In the structure of the robot, there are rotational joints and upper rolling joints. In Figure 4, the kinematic joints defined in the ADAMS dynamic model are detailed, namely:

- Joint A and Joint B are the rotational kinematic joints of the circular guide (4) with the robot housing. Joint A defines Motion 1, the law of motion for radial–ulnar deviation;
- Joint C is a rotational joint of the Hooke coupling structure;
- Joint D is a rotational joint of the bevel pinion with the system housing. This joint specifies Motion 2, the motion law for hand joint flexion–extension;
- Kinematic Joints R_1 and R_2, are superior joints that provide contact for a point on a curve. Special attention has been paid to the correct definition of the rolling joints between the circular guide and the slide. For this purpose, we have chosen to define a point-on-curve upper joint. In this case, for Joint R_1 we have specified the contact between the arc at the top of the guide and a point belonging to the slide. For Joint R_2, we have specified the contact between the arc of the circle at the bottom of the guide and a point belonging to the slide. These joints assure non-detaching contact between the circular guide (an arc of a circle) and the slide.

All other kinematic joints are defined according to the structural schematic shown in Figure 1, as detailed in Figure 4 on the ADAMS dynamic model.

✓ Another important step in the completion of the dynamic model is the definition of the toothed belt drive from the drive that performs ulnar–radial motion. For this purpose, we used the ADAMS machinery facility, which allows the definition of a toothed belt drive.

✓ Another step in finalizing the ParReEx robot model is to define the bevel gear.

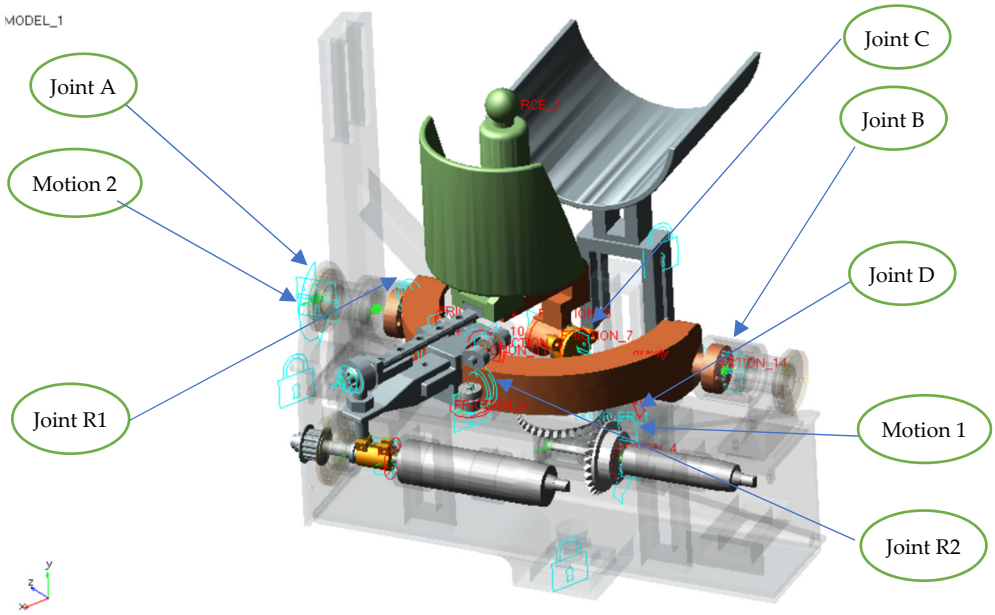

Figure 4. Kinematic joints defined in the ADAMS dynamic model.

For this purpose, we used the existing facility in Adams machinery to define gear drives. All the parameters required to define a bevel gear can be set in Table 1, namely: axis of rotation, number of teeth, face width, back cone distance, pitch angle, pitch apex, bore radius, outer module, addendum and dedendum factor.

Table 1. Bevel gear geometric parameters.

Parameter \ Value	Gear 1	Gear 2
No. of teeth	39	39
Orientation of rotation axis	0, 90, 0	90, 90, 0
Face width (mm)	25.4	25.4
Back cone distance (mm)	10	15
Pitch angle (°)	19.747	70.253
Pitch apex	0	0
Bore radius (mm)	2	2
Mean spiral angle (°) and direction	35, LH	35, RH
Outer trans. module (mm)	4.535	4.535
Tooth depth and width	Data Type I-ISO23509	
Profile shift coefficient	0.505	−0.505
Dedendum factor	1.25	1.25
Thickness mod. coef.	3.7×10^{-2}	-5.5×10^{-2}

The material properties of bevel gears are shown in Table 2. Further, on the bevel gear, the contact parameters between the tooth flanks are set, as shown in Table 3, namely: contact stiffness, contact exponent and damping coefficient.

Table 2. Bevel gear material properties.

Parameter \ Value	Gear1, Gear 2
Material type	Steel
Density (kg/m^3)	7801
Young's Modulus (N/m^2)	2.07×10^{11}
Poisson ratio	0.33

Table 3. Bevel gear contact parameters.

Parameter	Value
Stiffness (N/mm^2)	5×10^5
Contact exponent	1.1
Damping coefficient	5000
Penetration (mm)	0.01
Static friction coefficient	0.11
Static friction transition velocity (mm/s)	0.2
Dynamic friction coefficient	0.10
Dynamic friction transition velocity (mm/s)	0.5

The law-of-motion time-history diagram is shown in Figure 5. The two parameters, the amplitude of motion and the time period, were chosen taking into account the similarity between the laws of motion in numerical simulation and those recommended by therapists for proper physical rehabilitation. The two laws of motion that will be assisted by the robot are named in MSC.ADAMS as MOTION_1 and MOTION_2. These movements are defined using the STEP function, as shown below.

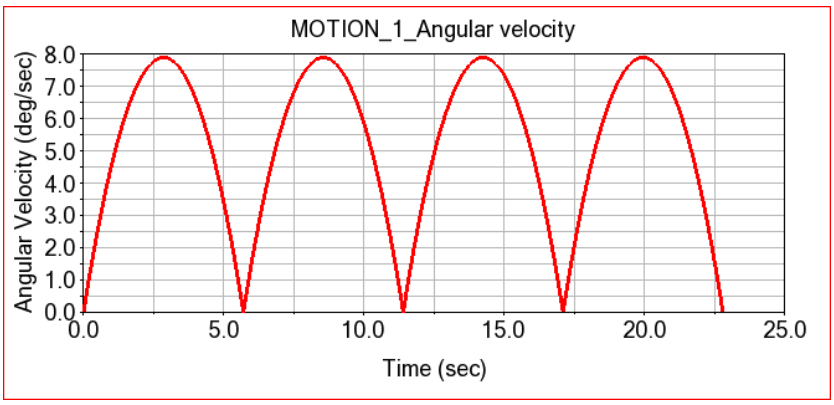

Figure 5. Law of motion imposed in ADAMS on ParReEx-wrist robot motor Joint E.

The law of MOTION 1, which corresponds to the flexion–extension movement, has a variation of $\pm 50^\circ$, with one step of the flexion movement performed in 5.7 s.

The law of MOTION 2 corresponds to ulnar–radial motion; it is specified on the same 5.7 s step, but the amplitude is 30 degrees.

MOTION 1: STEP (time, 0.0, 0.0d, 5.7, −50.0d) + STEP (time, 5.7, 0d, 11.4, 50.0d) + STEP (time, 11.4, 0.0d, 17.1, −50.0d) + STEP (time, 17.1, 0d, 22.8, 50.0d).

MOTION 2: STEP (time, 0.0, 0.0d, 5.7, 30.0d) + STEP (time, 5.7, 0d, 11.4, −30.0d) + STEP (time, 11.4, 0.0d, 17.1, 30.0d) + STEP (time, 17.1, 0d, 22.8, −30.0d).

The mannequin-rehabilitation robot assembly is dynamically analyzed in MSC.ADAMS with the two modules of the ParReEx-wrist robot (flexion/extension and radial–ulnar motion) active simultaneously for a period of 22.8 s. Figure 6 presents the two extreme operating positions of the ParReEx robot corresponding to the combined flexion–extension and ulnar–radial movements.

In the first phase, a dynamic simulation with the specified laws of motion and without considering the friction in the kinematic joints of the robot is performed. The results obtained for this simulation—meaning the variations of the motor torque calculated by numerical simulation in ADAMS when simultaneously performing both types of movement: flexion–extension and radial–ulnar motion of the wrist—are presented in Figure 7.

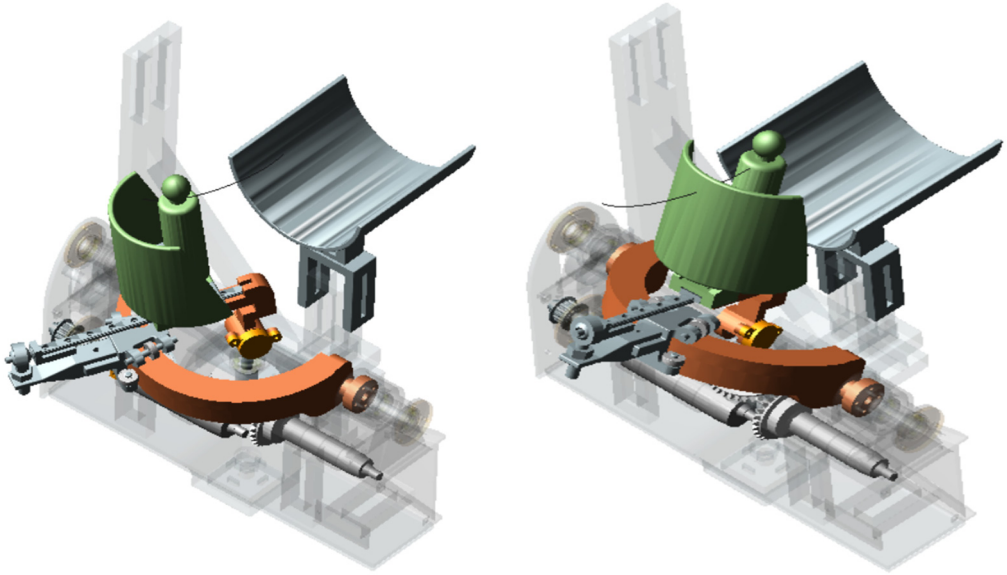

Figure 6. The two extreme positions during the operation of the virtual model of the ParReEx-wrist robot, corresponding to combined flexion–extension and radial–ulnar motion.

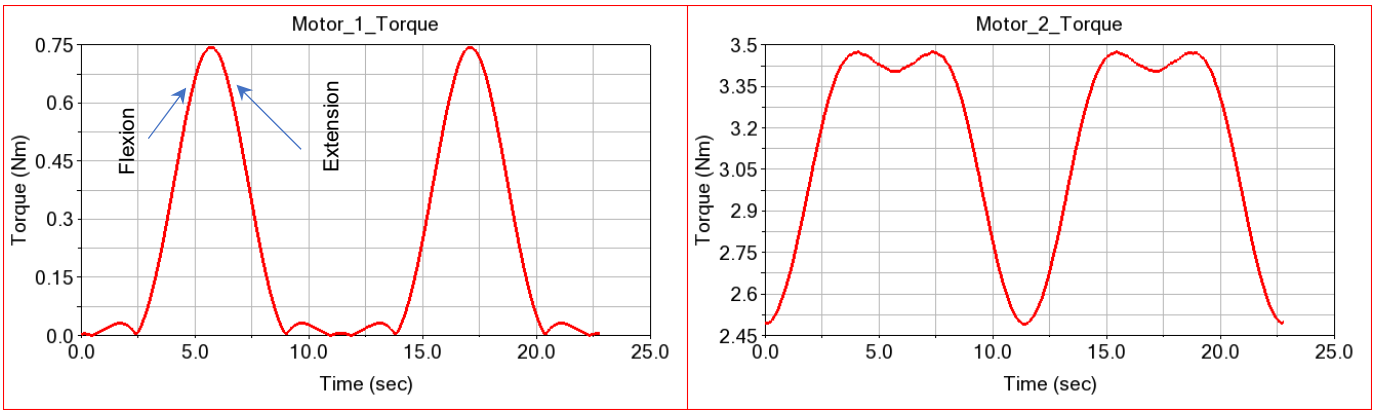

(**a**) (**b**)

Figure 7. ADAMS simulation computed torque for: (**a**) the flexion–extension module and (**b**) the radial–ulnar module.

Analyzing the graph in Figure 7a computed for the flexion–extension motion, it is found that the maximum value of the actuation moment of this flexion/extension module is 0.7436 Nm, while the minimum value is near 0 Nm.

The motor torque obtained by numerical simulation for the radial–ulnar motion (Figure 7b) has a maximum value around 3.4748 Nm and a minimum of 2.47 Nm. In conclusion, the radial–ulnar movement requires an actuation moment greater than about four times the moment required for the flexion–extension movement, so the flexion–extension module will be the most structurally loaded. For the two modules, the graphs of the connecting forces that develop in Joints A, B, R1, R2 and C are presented.

Figure 8 shows the orientation of the local reference axis systems attached to the kinematic torques of the ParReEx robot for clear identification of the components of the connecting forces.

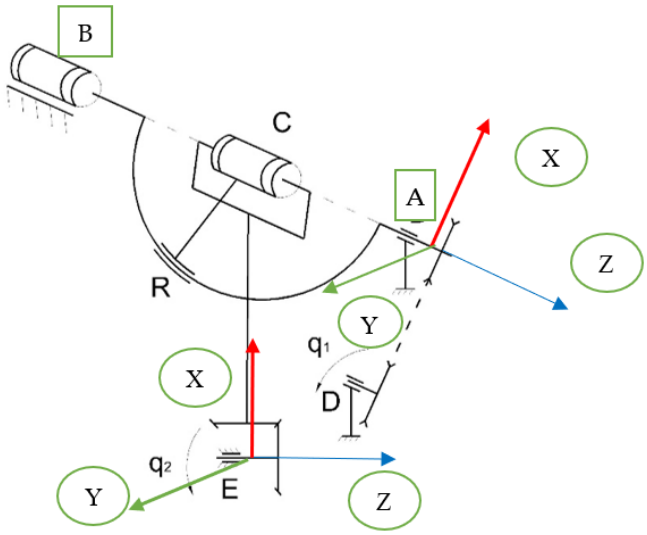

Figure 8. Positioning of the axes of the kinematic joints of the ParReEx robot.

Graphs of time variation for the components of the connecting force in Joint A in relation to the local reference system attached to this joint are shown in Figure 9a–c. Analysis of these graphs shows that the maximum value recorded along the Y-axis of the local reference system in Joint A is 111.7138 N, and the minimum is 60.8693 N, with an RMS (round mean square) equal to 95.1698 N (Figure 9b). The component along the X-axis reaches an absolute maximum value of 20.8049 N, and the minimum value is equal to 0.6315 N, with an RMS of 13.9479 N (Figure 9a). The component along the Z-axis reaches 88.6393 N with an RMS of 49.6273 N (Figure 9c). The value of the resulting force in this joint has a maximum of 142.1042 N and a minimum of 64.3436 N according to Figure 9d.

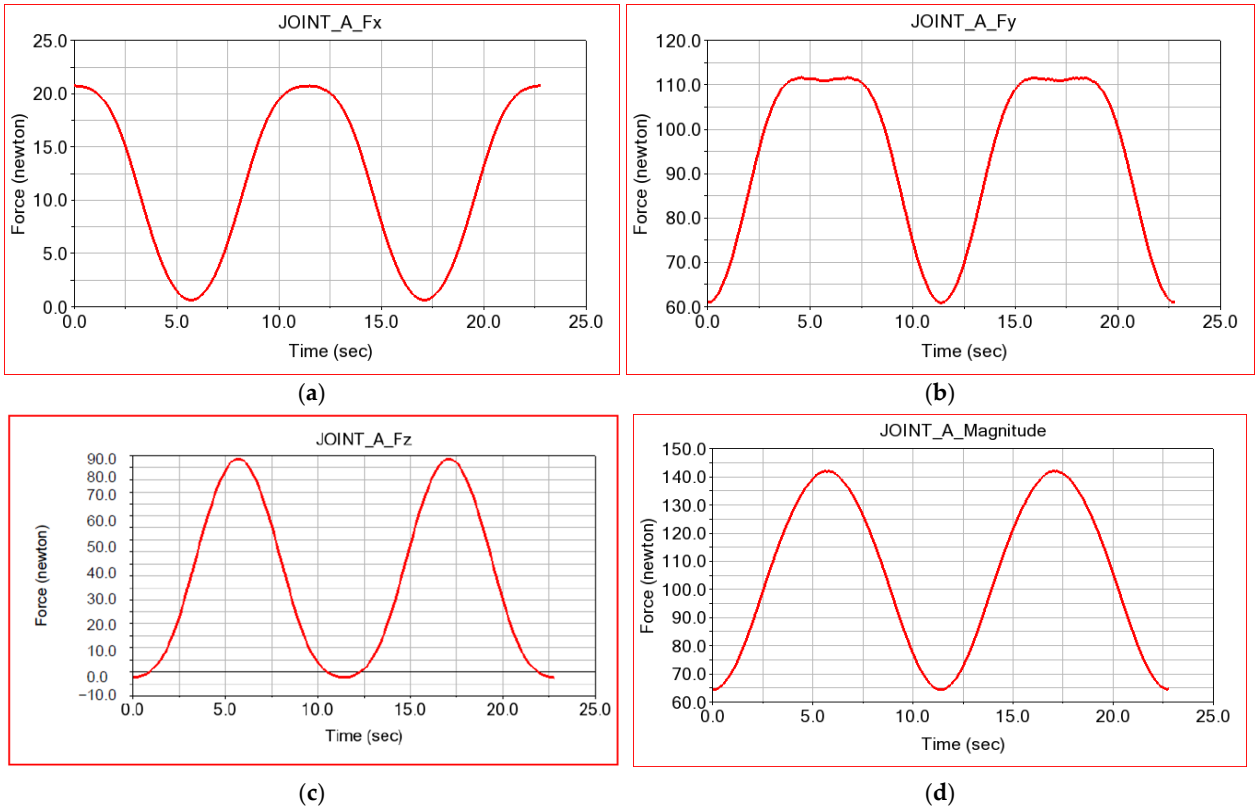

Figure 9. Connecting forces in rotation Joint A: (**a**) in the x-direction; (**b**) in the y-direction; (**c**) in the z-direction; and (**d**) the resultant.

These results are also presented in Table 4.

Table 4. Joint A connection force components.

Component / Parameter	Joint A Fx	Joint A Fy	Joint A Fz	Joint A MAG
Min	0.6315	60.8693	−2.4821	64.3436
Max	20.8049	111.7138	88.6393	142.1042
Avg	11.8015	93.2991	37.1483	104.7257
RMS	13.9479	95.1698	49.6273	108.2345

Graphs of time variation for the components of the connecting force in Joint B are shown in Figure 10a–c. The maximum value reported for the X-axis component is 25.8542 N, and the minimum is 11.002 N, with an RMS equal to 20.1699 N (Figure 10a). The Y-axis component has a maximum value equal to 0.3771 N, and the minimum value is equal to 0.2556 N, with an RMS of 0.3118 N (Figure 10b) The component along the Z-axis reaches 29.4384 N with an RMS of 24.3394 N (Figure 10c). The value of the resulting force in this joint reaches a maximum of about 32.6581 N, a minimum of 30.7333 N and an RMS equal to 31.6122 N, as we can see in Figure 10d.

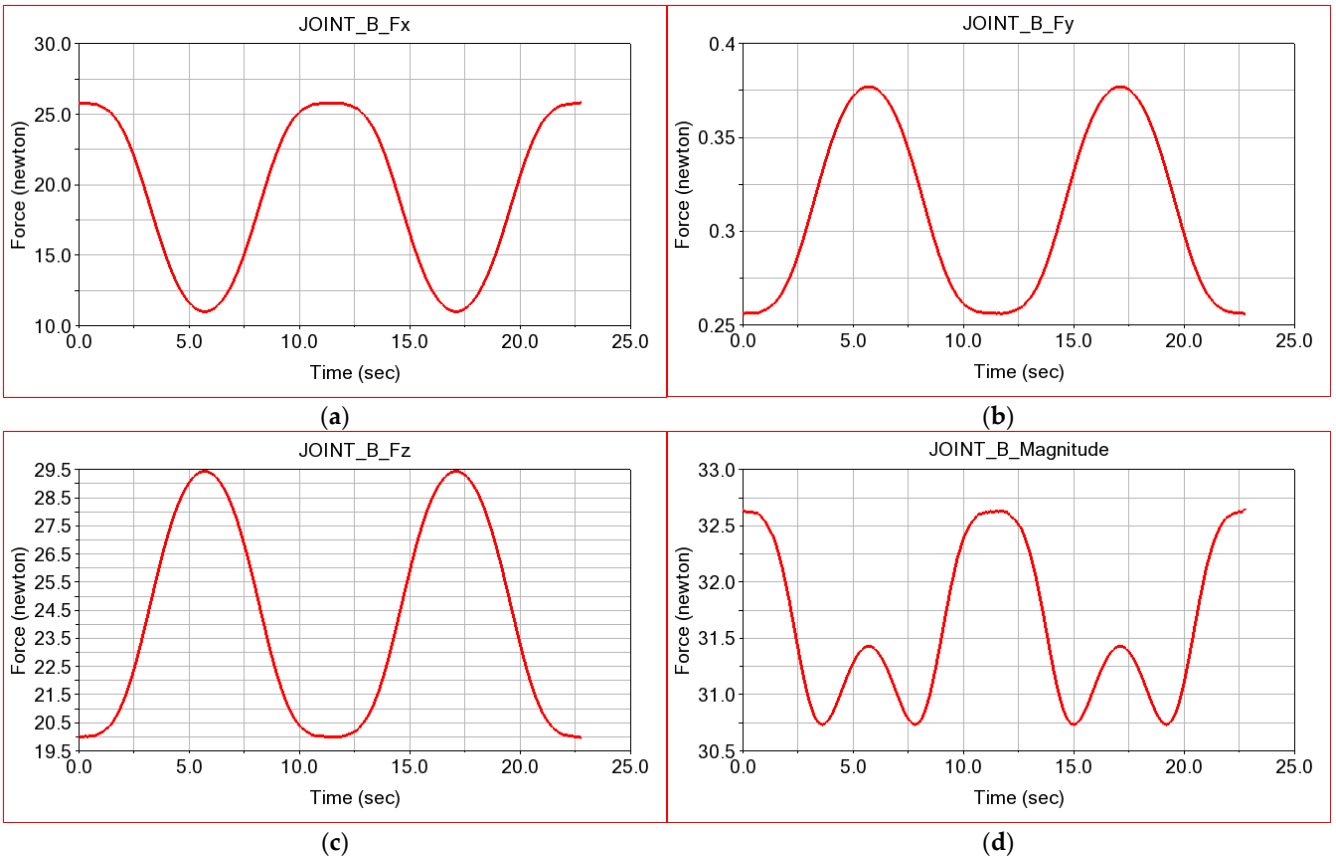

Figure 10. Connecting forces in rotational Joint B: (**a**) in the x-direction; (**b**) in the y-direction; (**c**) in the z-direction; and (**d**) the resultant.

These results are also shown in Table 5.

Table 5. Joint B connection force components.

Component / Parameter	Joint B Fx	Joint B Fy	Joint B Fz	Joint B MAG
Min	11.002	0.2556	19.9511	30.7333
Max	25.8542	0.3771	29.4384	32.6581
Avg	19.391	0.3084	24.0797	31.6122
RMS	20.1699	0.3118	24.3394	31.6122

There is a higher load distribution on Coupling A, i.e., the RMS value is 3.48 times higher for the force resulting from Joint A.

To model the contact between the radial bearings and the rolling path of the circular guide, we defined in ADAMS primitives such as the upper rolling torque between the outer ring of the bearing on the rolling path of the circular guide. The ParReEx robot has four bearings in the structure that make contact between the circular guide and the adjacent element.

Similar graphs are obtained for Joints R1 and R2 (Figures 11 and 12). The values of these results are presented in tabular form in Tables 6 and 7.

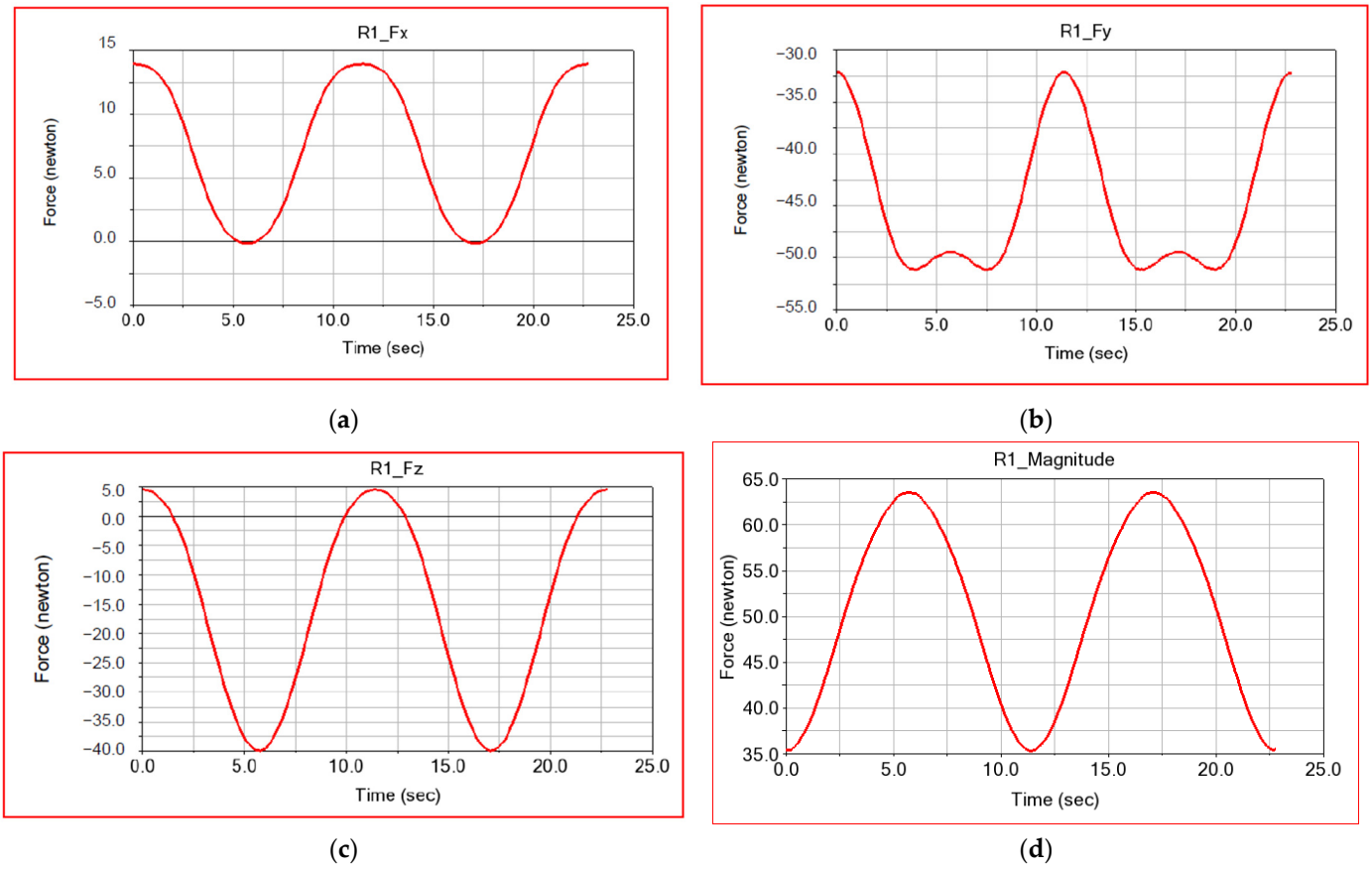

Figure 11. Connecting forces in rotational Joint R1: (**a**) in the x-direction; (**b**) in the y-direction; (**c**) in the z-direction; and (**d**) the resultant.

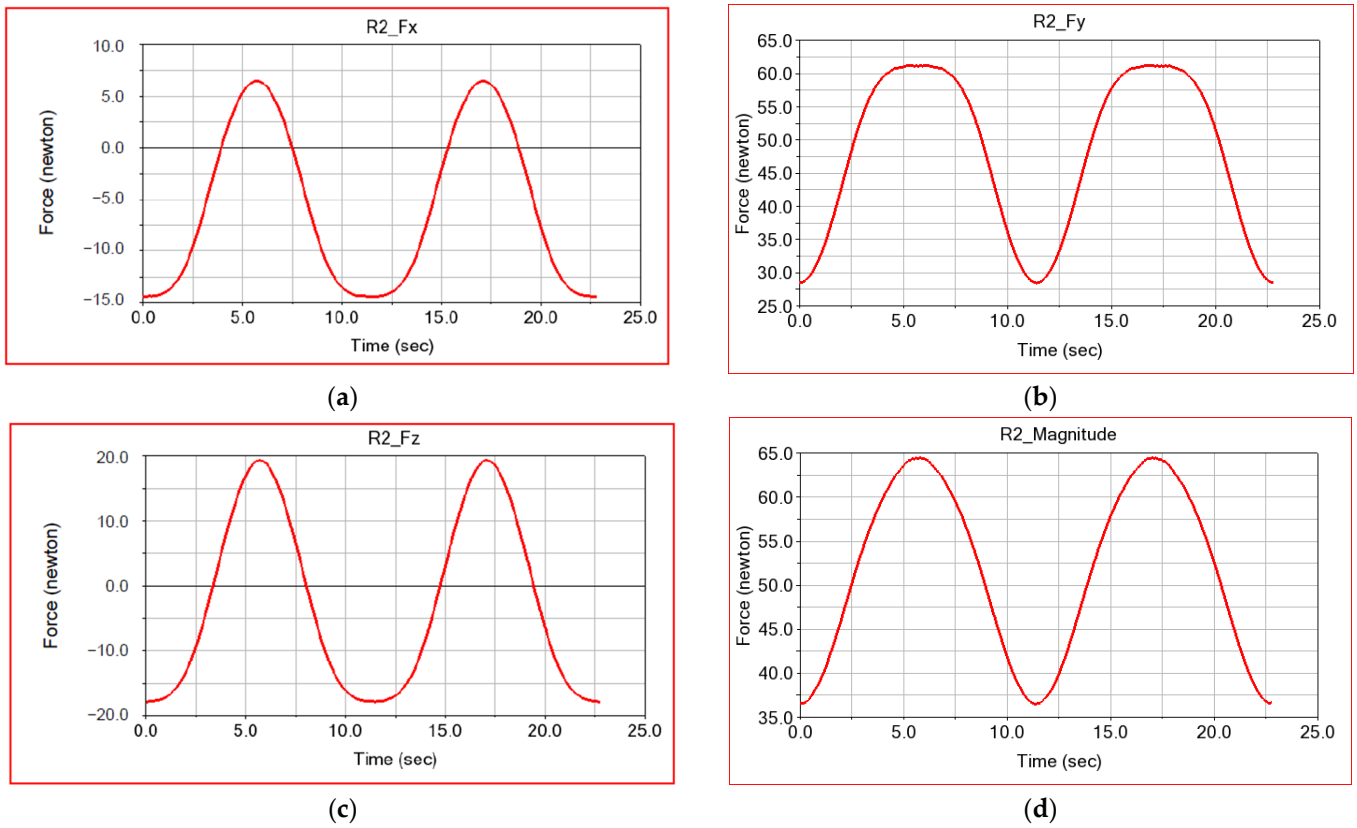

Figure 12. Connecting forces in rotational Joint R2 of the flexion/extension module: (**a**) in the x-direction; (**b**) in the y-direction; (**c**) in the z-direction; and (**d**) the resultant.

Table 6. Joint R1 connection force components.

Component / Parameter	Joint R1 Fx	Joint R1 Fy	Joint R1 Fz	Joint R1 MAG
Min	−0.1407	−51.1415	−39.9417	35.325
Max	13.994	−32.1514	4.533	63.5811
Avg	7.2739	−44.6805	−15.7091	50.263
RMS	8.9958	45.1932	22.3775	51.226

Table 7. Joint R2 connection force components.

Component / Parameter	Joint R2 Fx	Joint R2 Fy	Joint R2 Fz	Joint R2 MAG
Min	−14.4231	28.4593	−17.9002	36.502
Max	6.4731	61.2824	−19.281	64.5064
Avg	−5.6765	48.3102	−2.6405	21.6015
RMS	9.5789	49.7893	13.7125	52.39

For the situation in which the ParReEx robot is used by a patient and the frictional forces in the kinematic torques are not taken into account, the following results are obtained for the connecting forces in the Joint C, as presented in Figure 13.

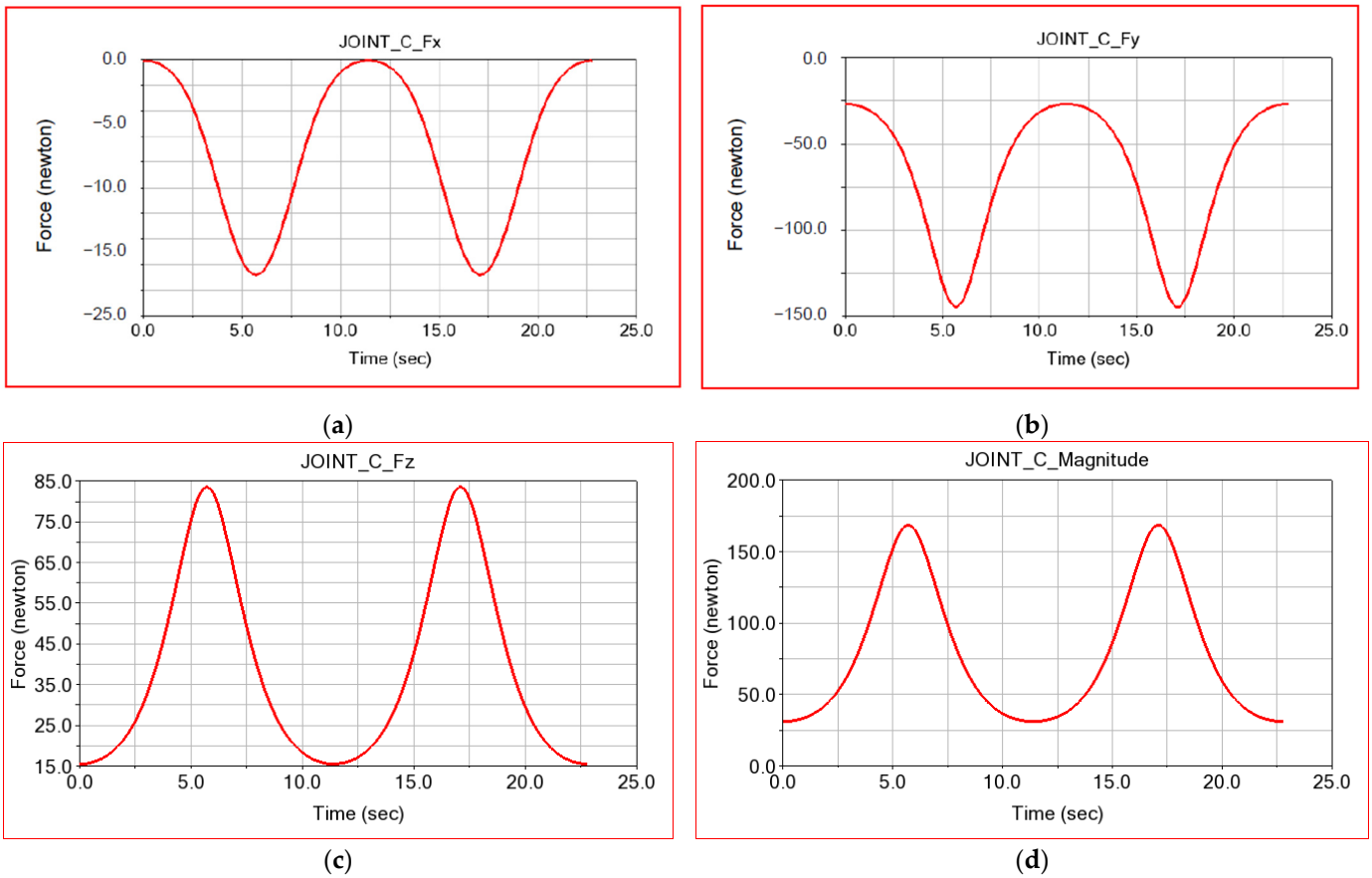

Figure 13. Connecting forces in rotational Joint C: (**a**) in the x-direction; (**b**) in the y-direction; (**c**) in the z-direction; and (**d**) the resultant.

Table 8 shows the values of the components and the resultant reaction in coupling C for the first case of study, i.e., without friction in the coupling and with the kinematic elements considered as rigid solids.

Table 8. Joint C connection force components.

Component / Parameter	Joint C Fx	Joint C Fy	Joint C Fz	Joint C MAG
Min	−20.9865	−144.671	15.4783	30.957
Max	−0.0759	−26.8092	85.5258	168.3648
Avg	−8.4707	−67.4532	38.9441	78.4077
RMS	11.2895	78.3566	45.2392	91.18

3.2. Dynamic Analysis in MSC.ADAMS of the ParReEx-Wrist Robot Considering Joint Friction

This subchapter is dedicated to a virtual dynamic study in ADAMS of the actuation moments and the connection forces in the kinematic Joints A, B, C, R1 and R2 considering the friction in the kinematic joints—a case that simulates the real situation and is different from the previous simulation in which simplistic hypotheses were used.

In principle, we are interested in simulating the dynamics of the robot in the context of its use by a patient. Therefore, in all dynamics studies, we consider this context.

To define the parameters required for the study of dynamics considering friction, existing data in the literature were used [50]. The following values were adopted for this study: static friction coefficient of 0.2 and dynamic friction coefficient of 0.15 (Table 9).

Table 9. Joint friction parameters.

Parameter	Value
Mu static	0.2
Mu dynamic	0.15
Friction arm (mm)	10
Bending friction arm (mm)	10
Pin radius (mm)	5
Stiction Transition velocity	0.1
Max. stiction deformation	0.01
Friction torque preload	0
Effect	Stiction only

Using numerical simulation in ADAMS considering the friction in joints, results were obtained in the form of laws of variation of the moments necessary to operate the flexion–extension module and the radial–ulnar deviation module (Figure 14).

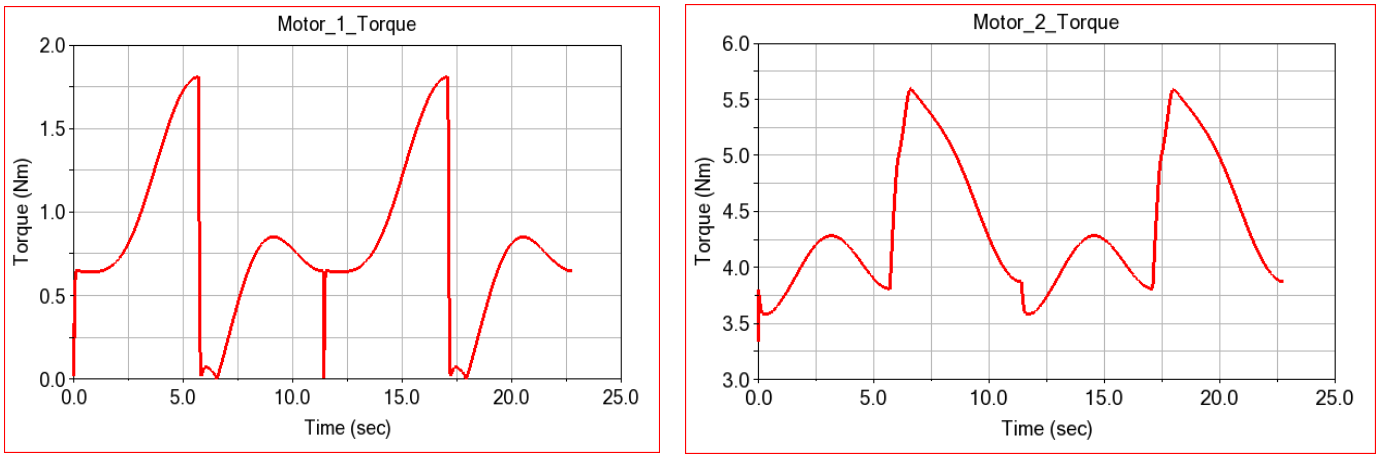

(**a**) (**b**)

Figure 14. Second case—ADAMS-simulation-computed torque for: (**a**) the flexion–extension module and (**b**) the radial–ulnar deviation module.

Table 10 shows the characteristic values for the actuation moments of the two robot modules for the second case study, namely when we considered the friction in the kinematic couplings.

Table 10. Robot motion parameters.

Component / Parameter	Motion 1 Torque (Nm)	Motion 2 Torque (Nm)
Min	0	0
Max	1.8086	5.5927
Avg	0.8143	4.3763
RMS	0.9317	4.4156

There is an increase in the motor torque required to operate the modules in this case, as well as a steeper variation, which is similar to that determined experimentally [18].

The graphs of the laws of variation of the connection forces considering friction as calculated in ADAMS are presented in Figure 15 for Joint A and in Figure 16 for Joint B.

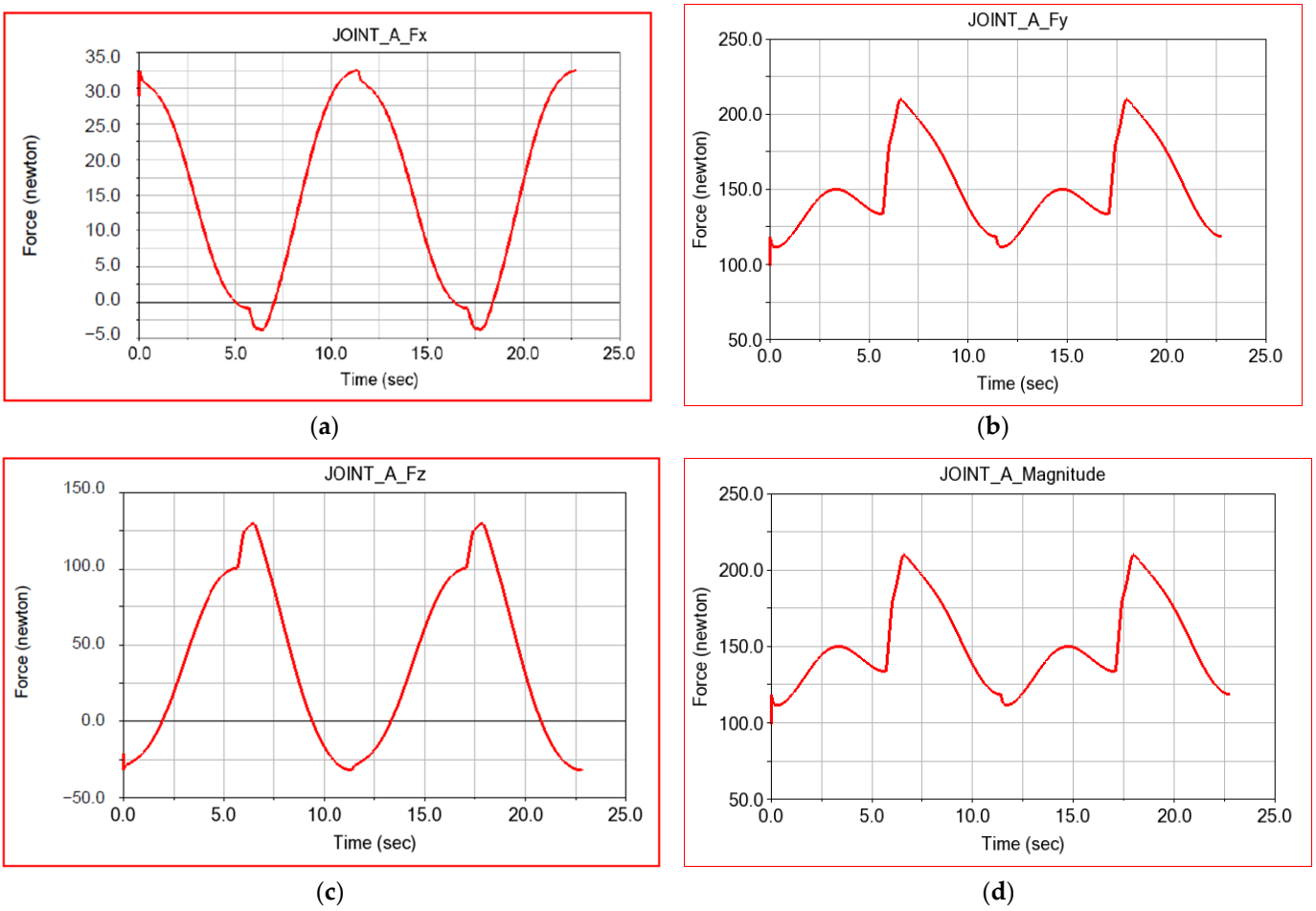

Figure 15. Connecting forces in rotation Joint A computed with friction consideration: (**a**) in the x-direction; (**b**) in the y-direction; (**c**) in the z-direction; and (**d**) the resultant.

The relevant results for the connecting force in Coupling A and its components are also given in Table 11.

Table 11. Joint A connection force components.

Component / Parameter	Joint A Fx	Joint A Fy	Joint A Fz	Joint A MAG
Min	−3.7855	99.3604	−32.0278	99.3604
Max	32.514	210.0206	129.7281	210.0206
Avg	15.0504	150.641	38.4032	150.641
RMS	19.5913	153.1624	65.5017	153.1624

We compare the results of the second simulation in the Discussion. The results obtained for Joint B in Case 2 are presented in Table 12.

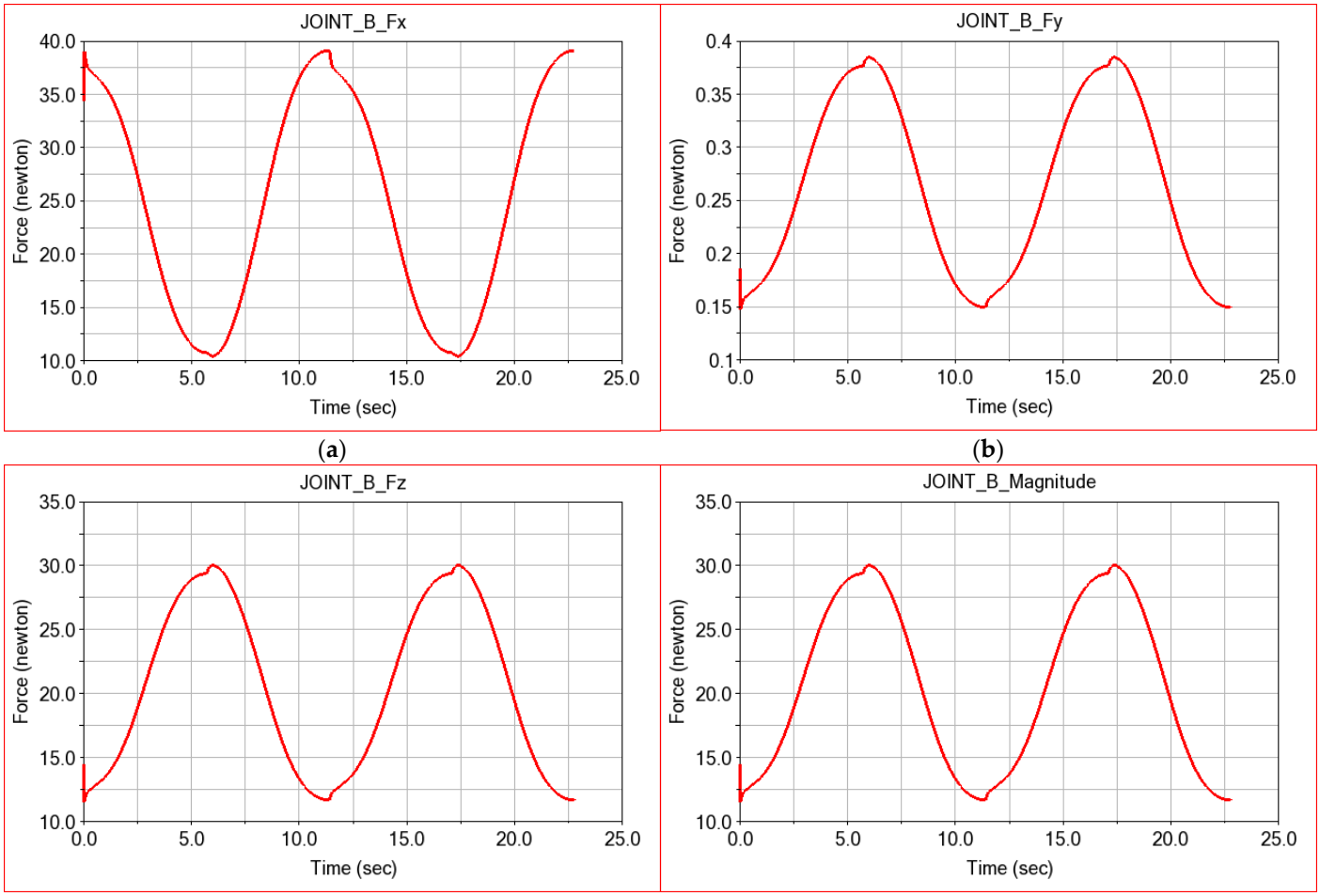

Figure 16. Connecting forces in Joint B calculated assuming friction: (**a**) in the x-direction; (**b**) in the y-direction; (**c**) in the z-direction; and (**d**) the resultant.

Table 12. Joint B connection force components.

Component / Parameter	Joint B Fx	Joint B Fy	Joint B Fz	Joint B MAG
Min	10.4354	0.1475	11.5174	11.5174
Max	39.1768	0.3846	30.0259	30.0259
Avg	24.8299	0.2639	20.6054	20.6054
RMS	26.8299	0.2767	21.6025	21.6025

To model the contact between the radial bearings and the circular guideway, we defined in ADAMS superior rolling couplings of the outer ring of the bearing on the circular guideway. The ParReEx robot has four bearings that ensure contact between the circular guide and the conjugate element.

Figure 17 shows the numerical results obtained by numerical simulation in ADAMS. View for the connection forces in the R1 coupling.

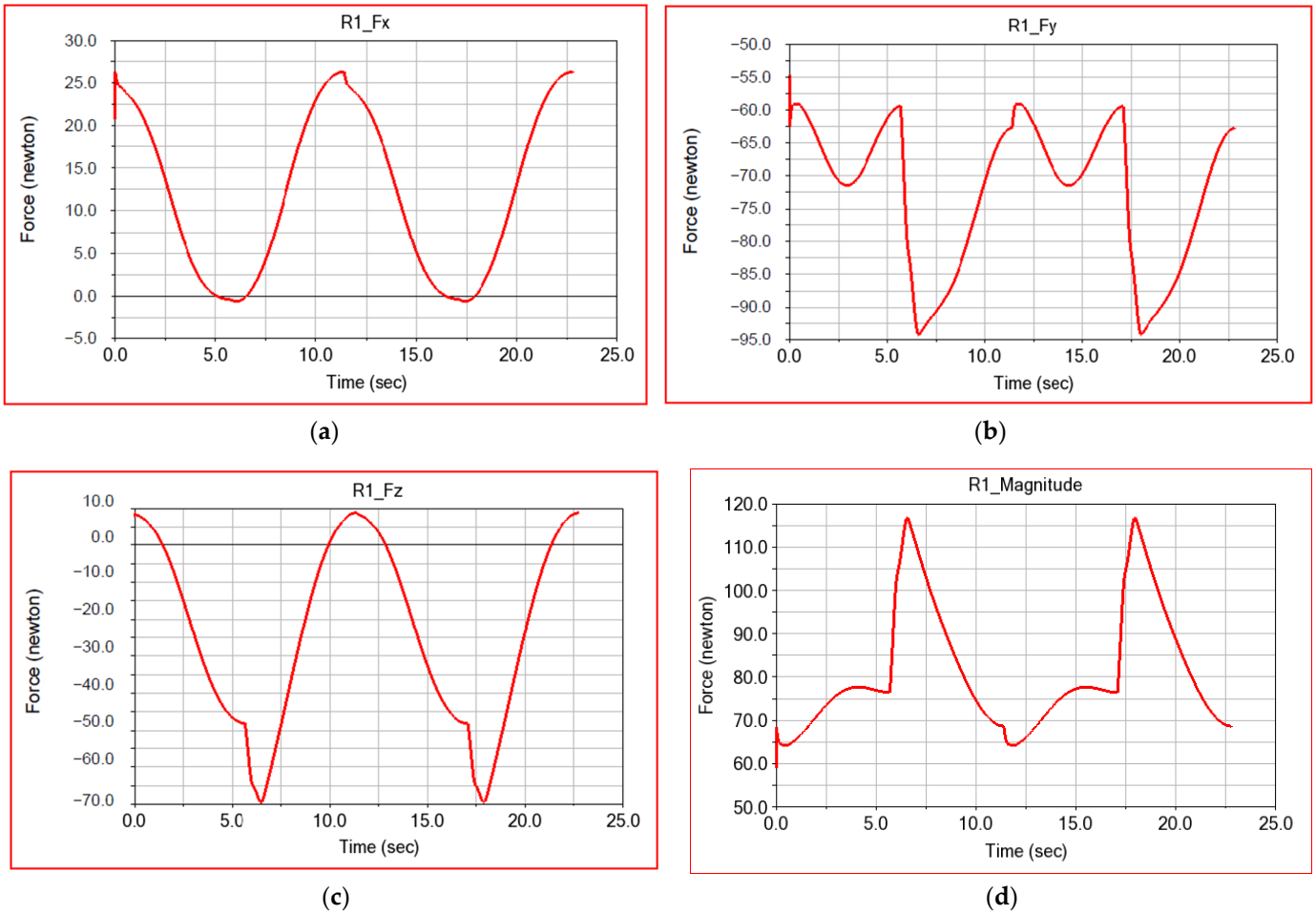

Figure 17. Connecting forces in rotational Joint R1: (**a**) in the x-direction; (**b**) in the y-direction; (**c**) in the z-direction; and (**d**) the resultant.

Table 13 shows the values of the components of the connection forces as well as the resulting reaction in the kinematic joint R1 for the second case study.

Table 13. Joint R1 connection force components.

Component / Parameter	Joint R1 Fx	Joint R1 Fy	Joint R1 Fz	Joint R1 MAG
Min	−0.6321	−94.2472	−69.4304	58.9881
Max	26.2981	−54.6674	8.8217	116.7565
Avg	11.9904	−72.4773	−23.7857	81.0712
RMS	15.3428	73.2824	34.1712	82.3006

Figure 18 shows the numerical results obtained by numerical simulation in ADAMS. View for the connection forces in the R2 coupling.

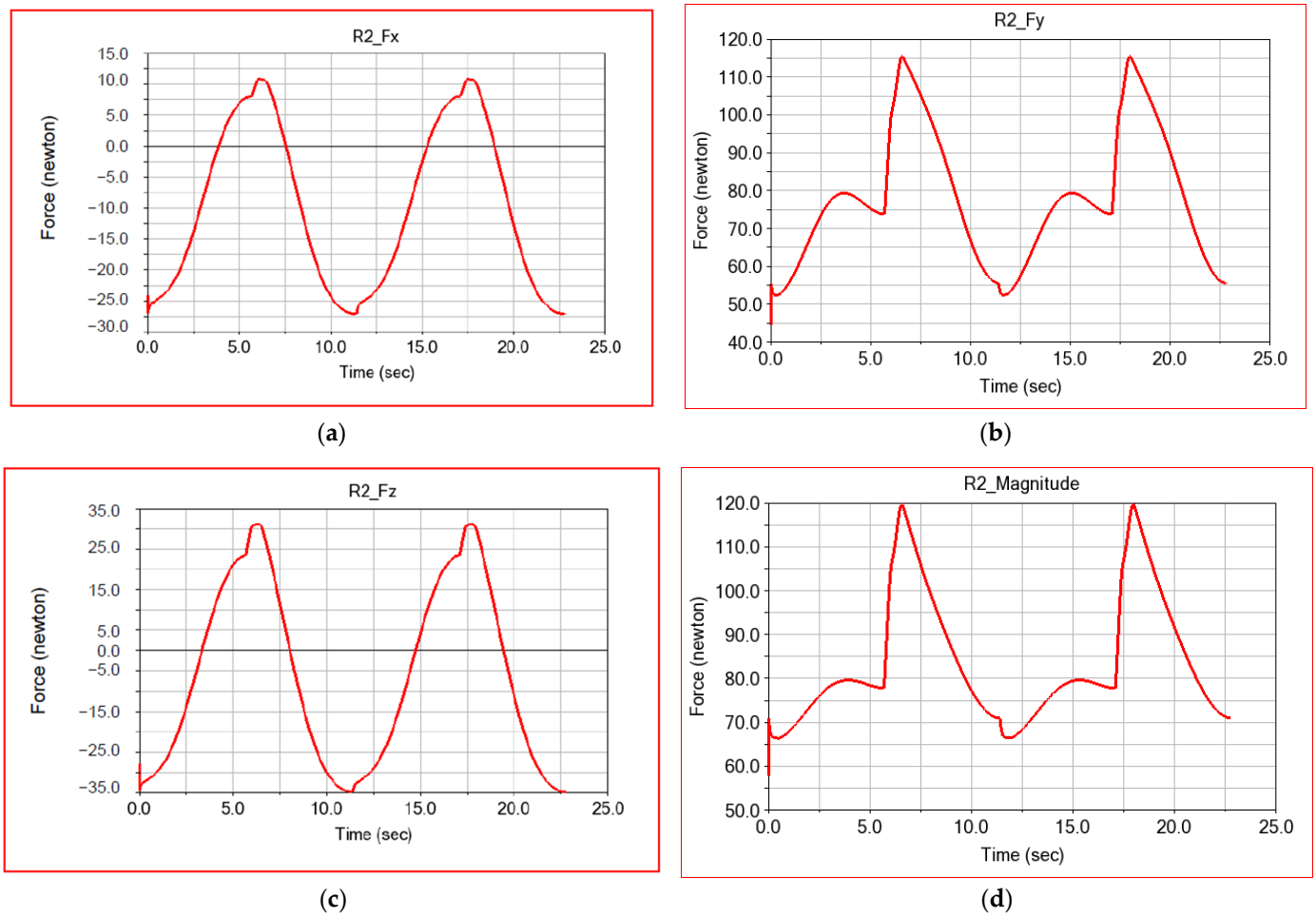

Figure 18. Connecting forces in rotational Joint R2: (**a**) in the x-direction; (**b**) in the y-direction; (**c**) in the z-direction; and (**d**) the resultant.

Table 14 shows the values of the components of the connection forces as well as the resulting reaction in the kinematic joint R2 for the second case study.

Table 14. Joint R2 connection force components.

Component / Parameter	Joint R2 Fx	Joint R2 Fy	Joint R2 Fz	Joint R2 MAG
Min	−27.1507	44.5072	−34.8471	57.757
Max	10.8219	115.4258	31.153	119.6574
Avg	−9.6479	77.8998	−5.9878	83.4607
RMS	16.3354	79.8368	23.0639	84.6918

For the situation when the ParReEx robot is used by a patient and we consider the frictional forces in the kinematic joints, the following results are obtained for connecting forces in Joint C, as presented in Figure 19.

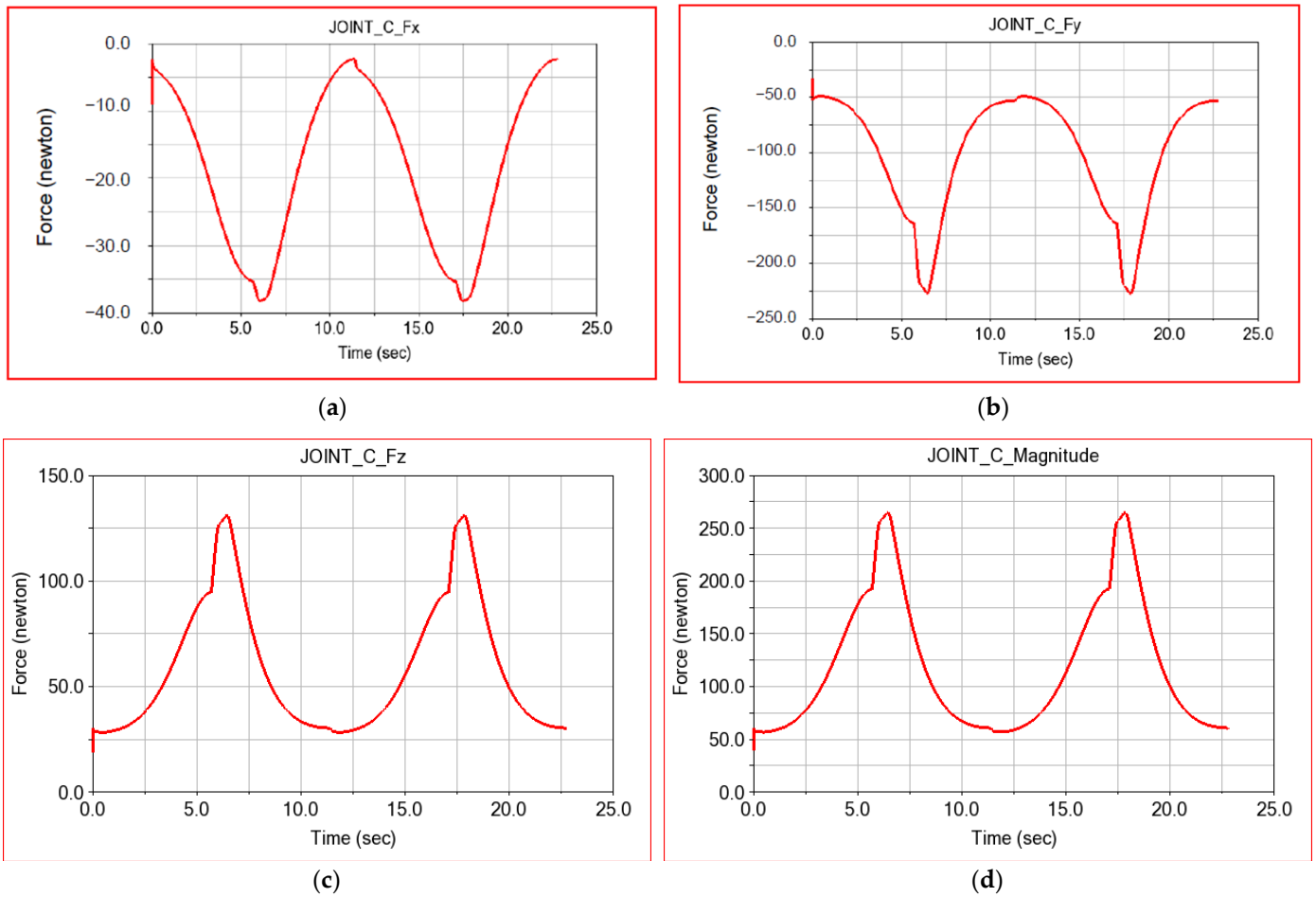

Figure 19. Connecting forces in rotational Joint C: (**a**) in the x-direction; (**b**) in the y-direction; (**c**) in the z-direction; and (**d**) the resultant.

Table 15 shows the values of the components of the connection forces as well as the resulting reaction in the kinematic joint C for the second case study.

Table 15. Joint C connection force components.

Component / Parameter	Joint C Fx	Joint C Fy	Joint C Fz	Joint C MAG
Min	−38.152	−226.9065	18.9705	39.0085
Max	−2.303	−32.8579	131.0045	264.6976
Avg	−18.3145	−101.217	58.4376	118.4064
RMS	21.8939	114.4402	66.0721	133.9455

For Joint A, the maximum RMS values increase from 108.2345 N in Case 1 (no joint friction) to 153.1624 N in Case 2 (with joint friction).

Numerical simulation in ADAMS is performed for the manikin-robot rehabilitation assembly considering friction in the rotating joints. The connection forces in the joints have obvious increases compared to the previously studied cases because friction plays an important role in the real operation of the robot.

3.3. Dynamic Analysis in MSC.ADAMS of the ParReEx-Wrist Robot Considering Flexible Elements and Joint Friction

This subchapter is dedicated to the virtual dynamic study in ADAMS of the actuation moments and the connection forces in kinematic joints A, B, C, R1 and R2 considering

friction in the kinematic joints and element flexibility, a case that simulates the real situation and is different from the first one, in which simplifying hypotheses have been used.

This simulation assumption is necessary because, in operation, the robot elements deform, and this influences the dynamic operating parameters. The way to transform a rigid body into a deformable one in ADAMS involves:

- Discretizing the body into finite elements and performing modal dynamics analysis, in which vibration modes are calculated based on modal superposition;
- Dynamic analysis considering the solid deformable body;
- Determination of torsional and flexural deformations of the flexible body.

Table 16 shows the vibration modes of the flexible element, namely the circular guide. Since in operation this element has the highest elasticity, it is very important to study the dynamics of the robot considering this circular guide as a deformable solid. Figure 20 shows that Vibration Mode 8 is flexural and occurs at 1538 Hz. Vibration modes consider the external connections of the element and can be flexural, torsional or a combination of the two.

Table 16. Circular guide modal parameters.

Mode Number	Frequency (Hz)	Mode Number	Frequency (Hz)
7	597.685	16	1.299×10^4
8	1538.863	17	1.546×10^4
9	1828.696	18	2.315×10^4
10	2804.835	19	2.827×10^4
11	3835.677	20	2.987×10^4
12	4032.088	21	6.923×10^4
13	5993.852	22	8.053×10^4
14	6743.001	23	1.343×10^5
15	9246.1609	24	1.808×10^5

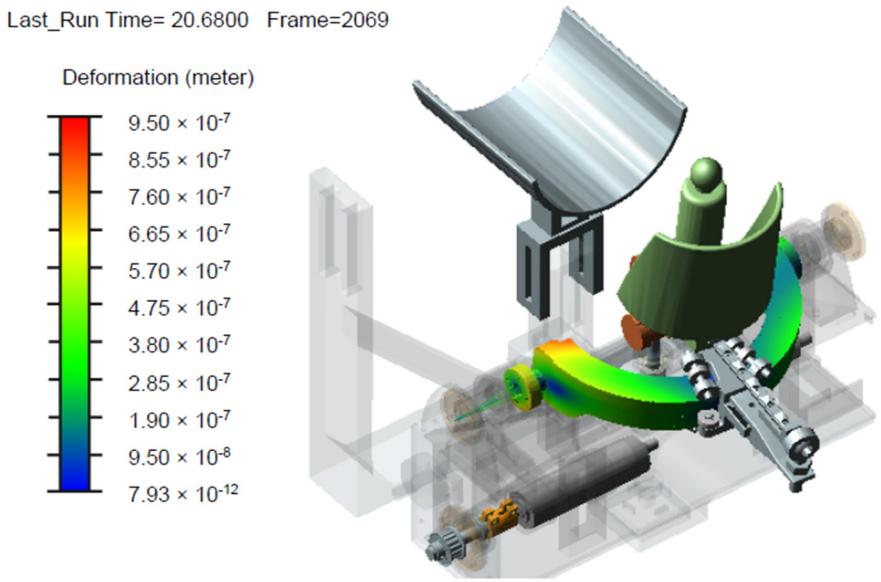

Figure 20. The deformable body in ADAMS and view of body deformation map.

Numerical simulation in ADAMS considering the friction in joints and the flexibility of the circular guide element resulted in laws of variation of the torque necessary to operate the flexion–extension module as well as the radial–ulnar module (Figure 21).

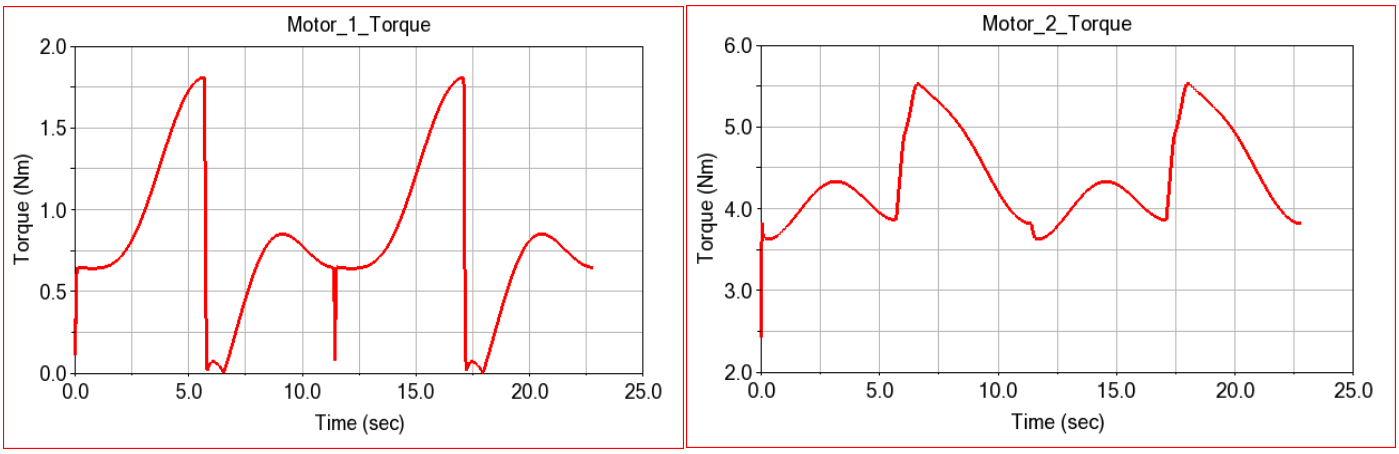

(**a**) (**b**)

Figure 21. The laws of variation of computed torque for: (**a**) the flexion–extension module and (**b**) the radial–ulnar module.

There is an increase in the motor torque required to operate the modules in this case as well as a steeper variation, similar to values determined experimentally [18].

In Table 17, the characteristic values for the actuation moments of the two modules of the robot are presented for case 3 of the study, i.e., considering the flexibility of the elements and the friction in the couplings.

Table 17. Robot motion parameters in Case 3.

Component / Parameter	Motion 1 Torque	Motion 2 Torque
Min	0.0013	2.431
Max	1.8086	5.5339
Avg	0.8143	4.3712
RMS	0.9316	4.4062

Figure 22 shows the laws of variation for the components of the connection forces in coupling A as well as for the resultant reaction. These results are obtained in case 3 of the simulation, i.e., the one in which we considered simultaneously the friction in the kinematic couplings and the flexibility of the elements.

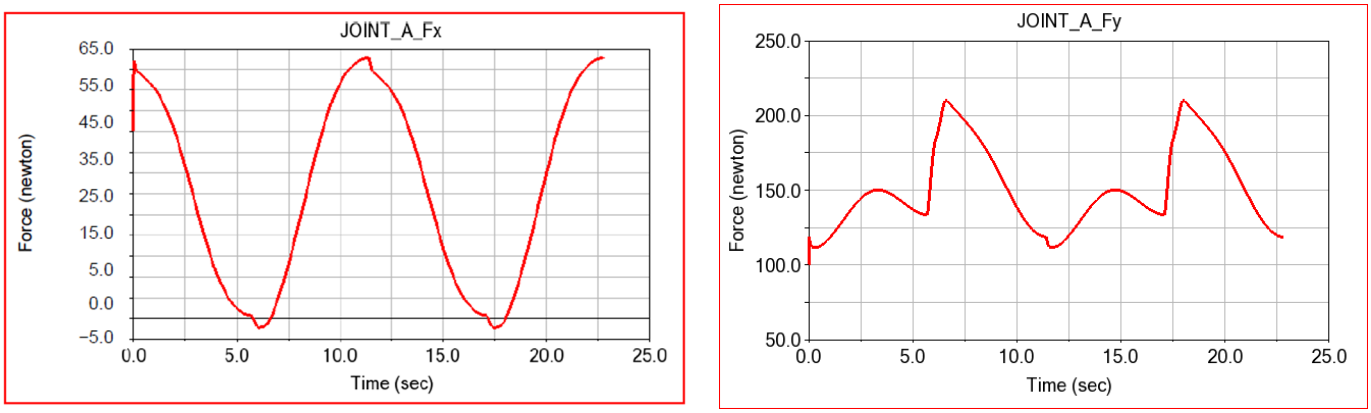

(**a**) (**b**)

Figure 22. *Cont.*

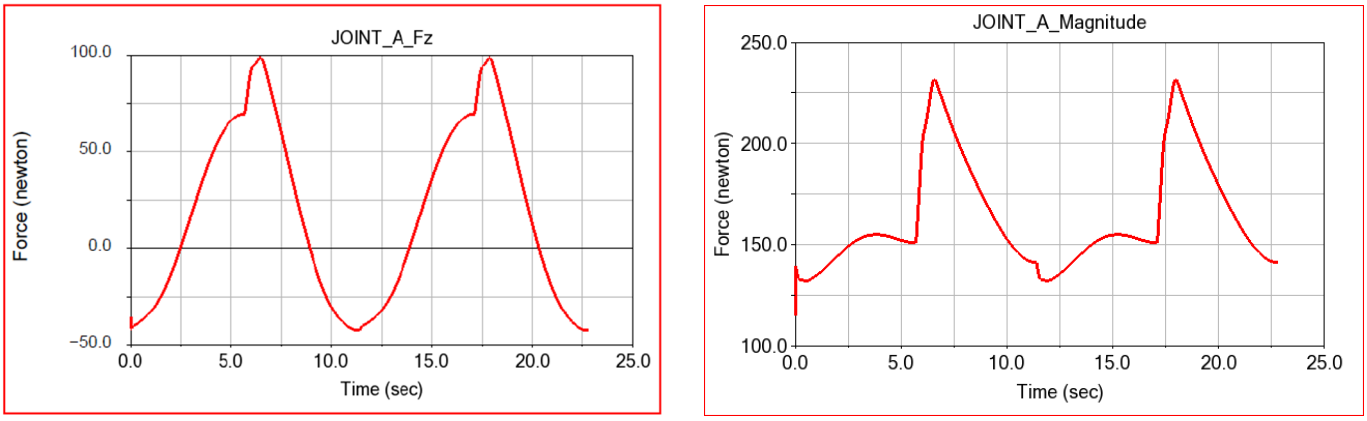

(**c**) (**d**)

Figure 22. Connecting forces in rotation Joint A computed with friction and flexible links: (**a**) in the x-direction; (**b**) in the y-direction; (**c**) in the z-direction; and (**d**) the resultant.

Table 18 shows the numerical results obtained for the components of the forces and the resulting reaction in joint A for simulation case 3.

Table 18. Joint A connection force components.

Parameter \ Component	Joint A Fx	Joint A Fy	Joint A Fz	Joint A MAG
Min	−2.2236	99.6565	−42.8897	115.1857
Max	62.8521	210.1286	98.7351	231.5797
Avg	30.9324	150.7614	17.3479	163.231
RMS	38.4147	153.2828	48.9964	165.4441

Figure 23 shows the laws of variation for the components of the connection forces in coupling B as well as for the resultant reaction, for the third simulation case.

Table 19 shows the numerical results obtained for the components of the forces and the resulting reaction in joint B for simulation case 3.

Table 19. Joint B connection force components.

Parameter \ Component	Joint B Fx	Joint B Fy	Joint B Fz	Joint B MAG
Min	0.4806	−0.8625	−1.6387	0.4815
Max	9.1875	0.4868	1.0018	9.2307
Avg	8.8505	0.4033	−0.4287	8.91
RMS	8.853	0.4095	0.9483	8.9131

Figure 24 shows the laws of variation for the components of the connection forces in coupling R1 as well as for the resultant reaction, for the third simulation case.

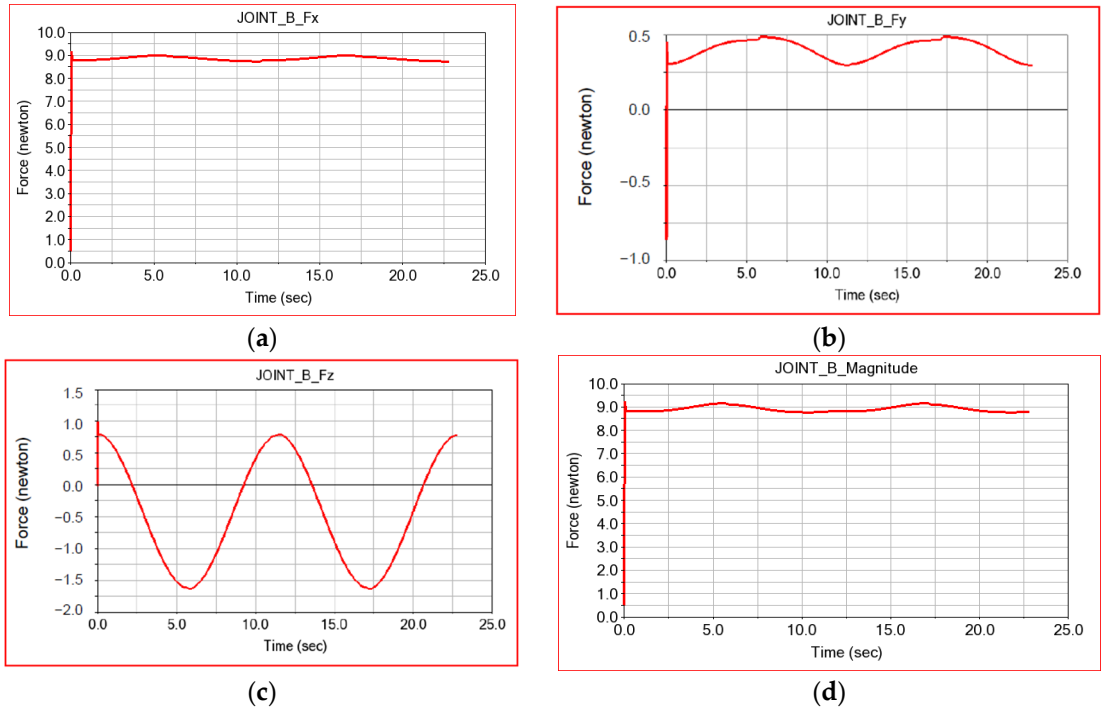

Figure 23. Connecting forces in Joint B calculated assuming friction and flexible links: (**a**) in the x-direction; (**b**) in the y-direction; (**c**) in the z-direction; and (**d**) the resultant.

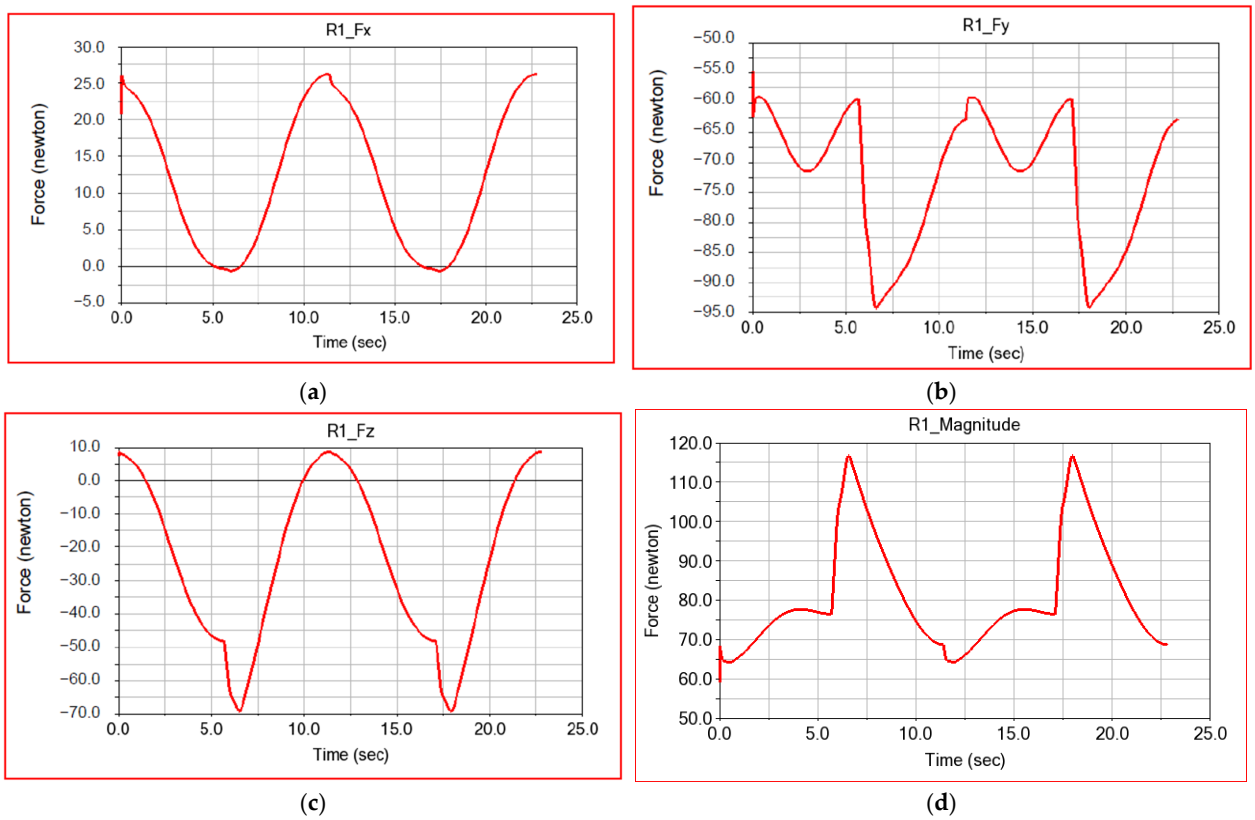

Figure 24. Connecting forces in rotational Joint R1 in Case 3: (**a**) in the x-direction; (**b**) in the y-direction; (**c**) in the z-direction; and (**d**) the resultant.

Table 20 shows the numerical results obtained for the components of the forces and the resulting reaction in joint R1 for simulation case 3.

Table 20. Joint R1 connection force components.

Component / Parameter	Joint R1 Fx	Joint R1 Fy	Joint R1 Fz	Joint R1 MAG
Min	−0.6319	−94.247	−69.4296	59.116
Max	26.2983	−54.7853	8.8217	116.7565
Avg	11.2983	−72.4702	−23.7732	81.0625
RMS	15.3456	73.4702	34.1647	82.2926

Figure 25 shows the laws of variation for the components of the connection forces in coupling R2 as well as for the resultant reaction, for the third simulation case.

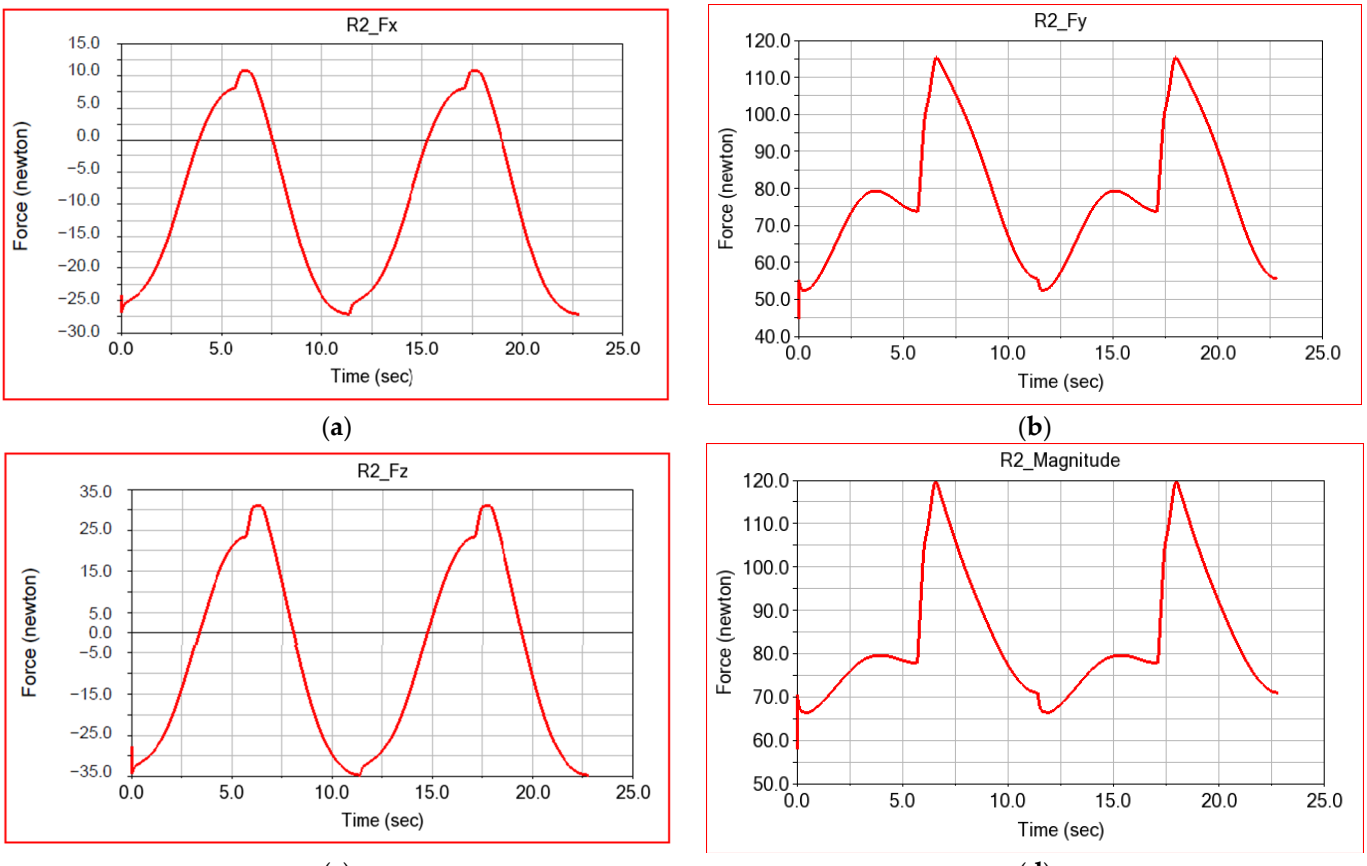

Figure 25. Connecting forces in rotational Joint R2 in Case 3: (**a**) in the x-direction; (**b**) in the y-direction; (**c**) in the z-direction; and (**d**) the resultant.

Table 21 shows the numerical results obtained for the components of the forces and the resulting reaction in joint R2 for simulation case 3.

Table 21. Joint R2 connection force components.

Component / Parameter	Joint R2 Fx	Joint R2 Fy	Joint R2 Fz	Joint R2 MAG
Min	−27.1509	44.6085	−34.8469	57.8858
Max	10.8215	115.425	31.1528	119.6571
Avg	−9.6539	77.8865	−5.9965	83.4504
RMS	16.3394	79.8258	23.066	84.6827

For the situation when the ParReEx robot is used by a patient considering the frictional forces in the kinematic joints and the flexibility of the elements, the following results are obtained for connecting forces in Joint C, as shown in Figure 26.

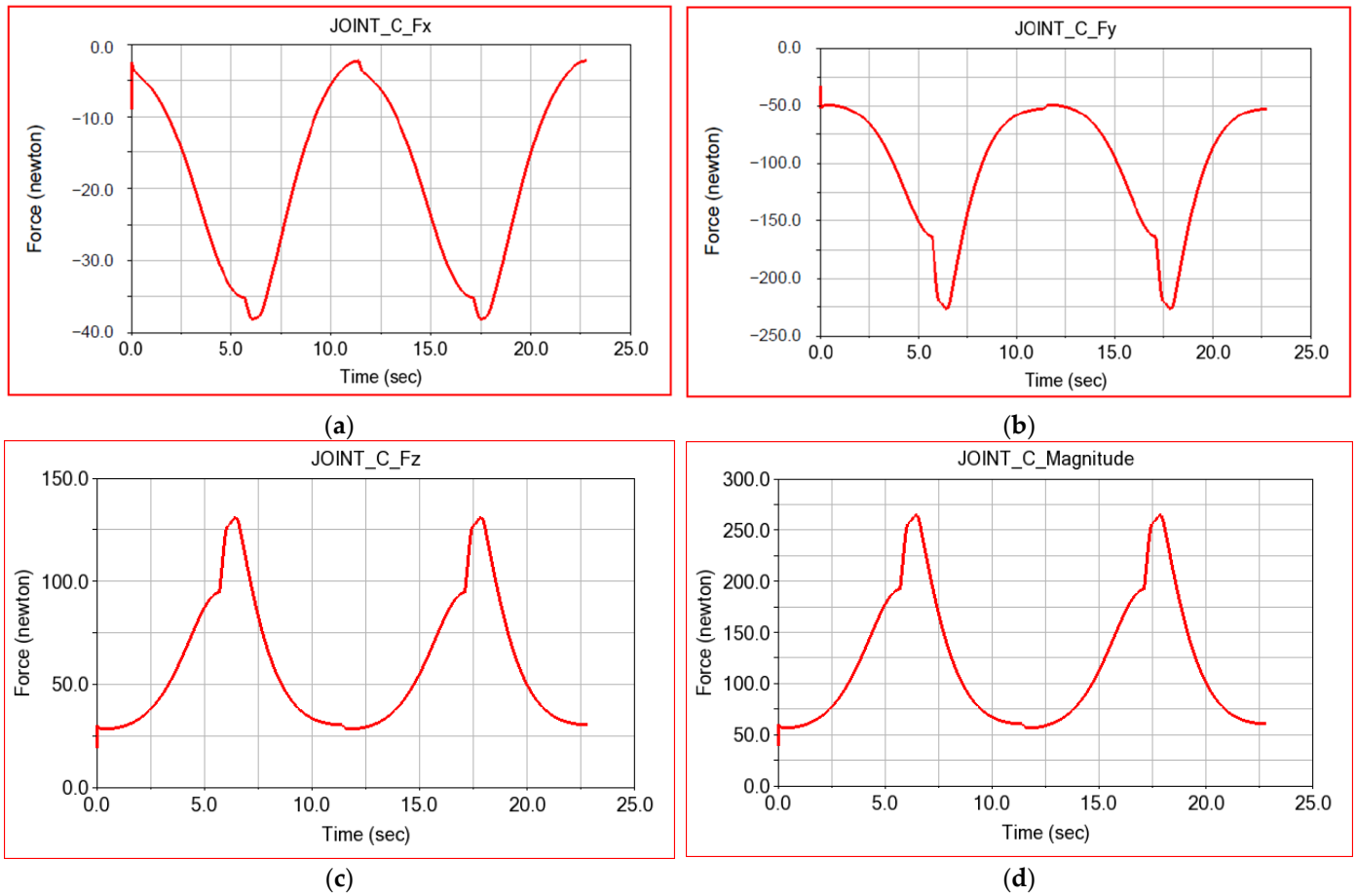

Figure 26. Connecting forces in rotational Joint C in Case 3: (**a**) in the x-direction; (**b**) in the y-direction; (**c**) in the z-direction; and (**d**) the resultant.

Table 22 shows the numerical results obtained for the components of the forces and the resulting reaction in joint C for simulation case 3.

Table 22. Joint C connection force components.

Component / Parameter	Joint C Fx	Joint C Fy	Joint C Fz	Joint C MAG
Min	−38.152	−226.9063	19.031	39.1179
Max	−2.3031	−32.9627	131.0044	264.6962
Avg	−18.3109	−101.1899	58.422	118.375
RMS	21.8903	114.4194	66.0601	133.9213

As previously specified, in this simulation case, we are interested in the translational displacements associated with the marker attached to the center of mass of the circular guide relative to its undeformed location. In addition to the displacements, we are also interested in the specific deformations of this marker. These results are shown in Figures 27 and 28.

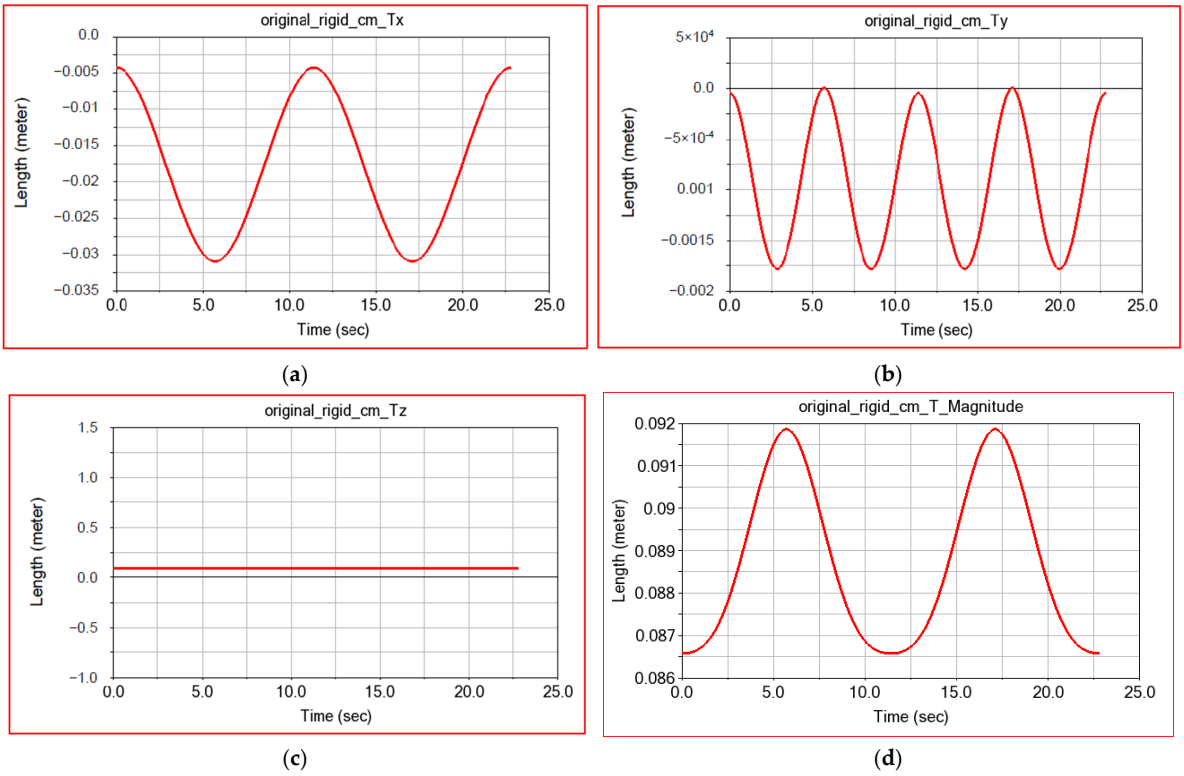

Figure 27. Displacement of the center of mass of the circular guide: (**a**) in the x-direction; (**b**) in the y-direction; (**c**) in the z-direction; and (**d**) the resultant.

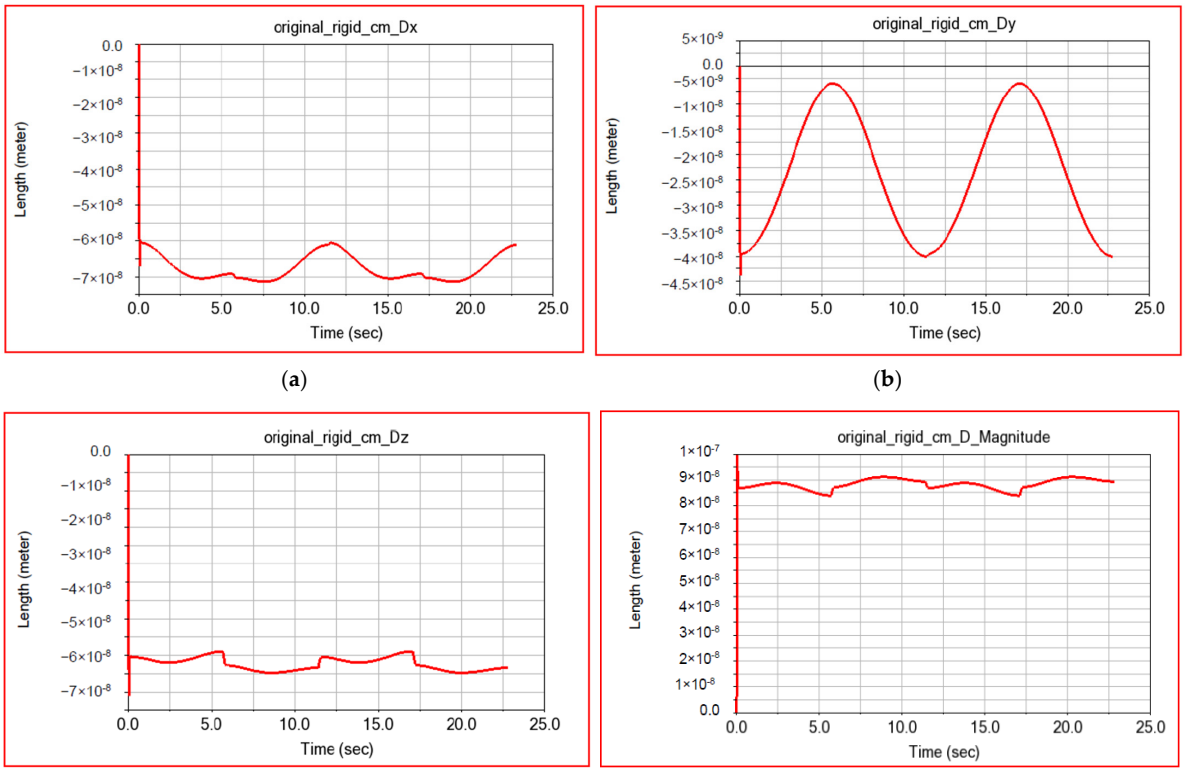

Figure 28. Deformation of the center of mass of the circular guide: (**a**) in the x-direction; (**b**) in the y-direction; (**c**) in the z-direction; and (**d**) the resultant.

Table 23 shows the numerical results obtained for the components and the resulting displacement of the marker attached to the center of mass of the circular guide.

Table 23. Displacement of the center of mass of the circular guide.

Parameter \ Component	Depl Tx (m)	Depl Ty(m)	Depl Tz(m)	Depl T Mag(m)
Min	−0.031	−0.0018	0.0865	0.0866
Max	−0.0042	7.620×10^{-6}	0.0865	0.0919
Avg	−0.0176	-9.243×10^{-4}	0.0865	0.0887
RMS	0.0199	0.0011	0.0865	0.0887

Table 24 shows the numerical results obtained for the components and the resulting deformations of the marker attached to the center of mass of the circular guide.

Table 24. Deformation of the center of mass of the circular guide.

Parameter \ Component	Def Dx(m)	Def Dy(m)	Def Dz(m)	Def D Mag(m)
Min	-6.638×10^{-8}	-4.132×10^{-8}	-6.603×10^{-8}	2.46×10^{-11}
Max	-1.948×10^{-11}	1.405×10^{-11}	-3.737×10^{-12}	9.960×10^{-8}
Avg	-6.256×10^{-8}	-2.094×10^{-8}	-5.735×10^{-8}	8.83×10^{-8}
RMS	6.268×10^{-8}	2.412×10^{-8}	5.739×10^{-8}	8.834×10^{-8}

A map of the specific strain distribution of the robot's circular guide is shown in Figure 29. These deformations have very small values, so this guide is designed with sufficient stiffness. Its mass can be reduced by structural stiffening, which will be discussed in the next paragraph.

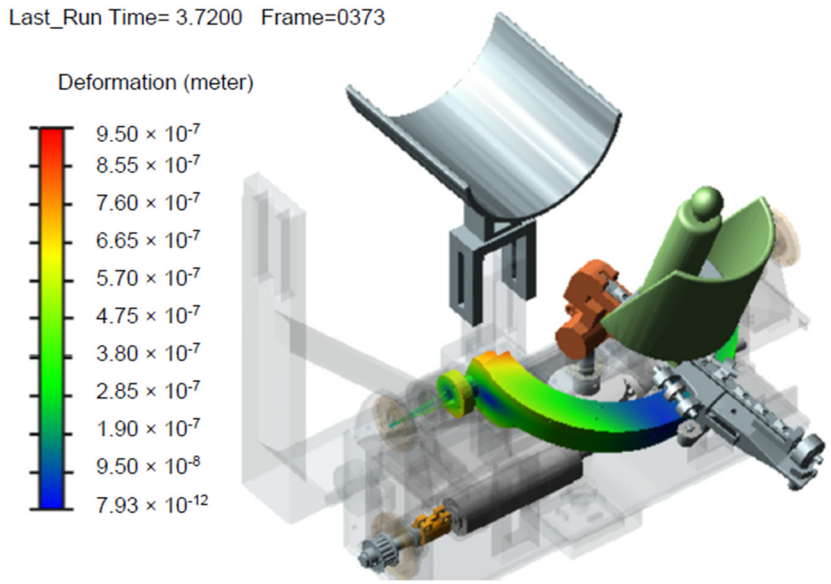

Figure 29. Deformation map of the robot circular guide.

4. Structural Optimization of the Circular Guide of the ParReEx Robot

The circular guide in the structure of the ParReEx robot is an important part that must maintain a certain torsional and bending rigidity and a corresponding resistance to fatigue. To achieve structural optimization of the circular guide, we start from its existing geometry, which we model parametrically with the help of the ANSYS Workbench-Design Modeler preprocessor, as shown in Figure 30.

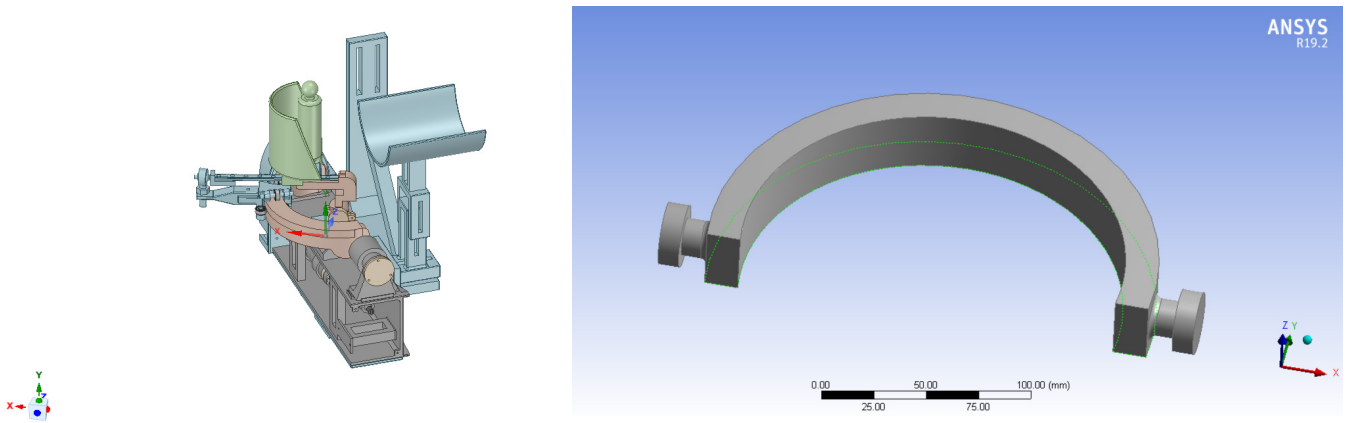

Figure 30. Parameterized model of the circular guide in ANSYS Design Modeler.

Structural optimization involves two objectives:

- Reducing the mass of the circular guide, which is made of aluminum alloy, by respecting the constraint of a maximum equivalent stress;
- Increased fatigue resistance by reducing peak tensions in areas with stress concentrators. These areas are the two spindles through which the guide is supported in the bearing housings.

The optimization block diagram is shown in Figure 31.

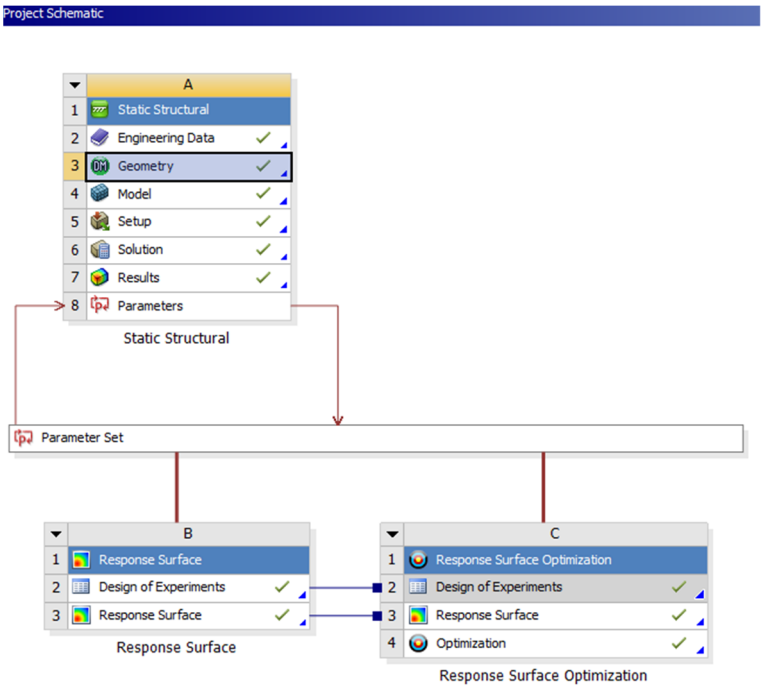

Figure 31. Block diagram of the structural optimization process of the guide.

The steps of the structural optimization process of the circular guide in accordance with the block diagram in Figure 31 are described in the following.

4.1. Parameterized Geometric Modelling of Circular Guidance Using the Design Modeler Preprocessor

Three geometrical parameters of the guide are selected as input data, namely: the radii of the two spindles connecting the circular guide, and the inner radius of the guide, named R1, as shown in Figure 32. At this stage, the physically possible ranges of variation of the

geometrical parameters included in the optimization process are checked and determined. Thus, the range of variation of the two radii is between 2.7 and 3.3 mm. For the inner radius of the circular guide, the variation limits are from 82.8 to 101.2 mm.

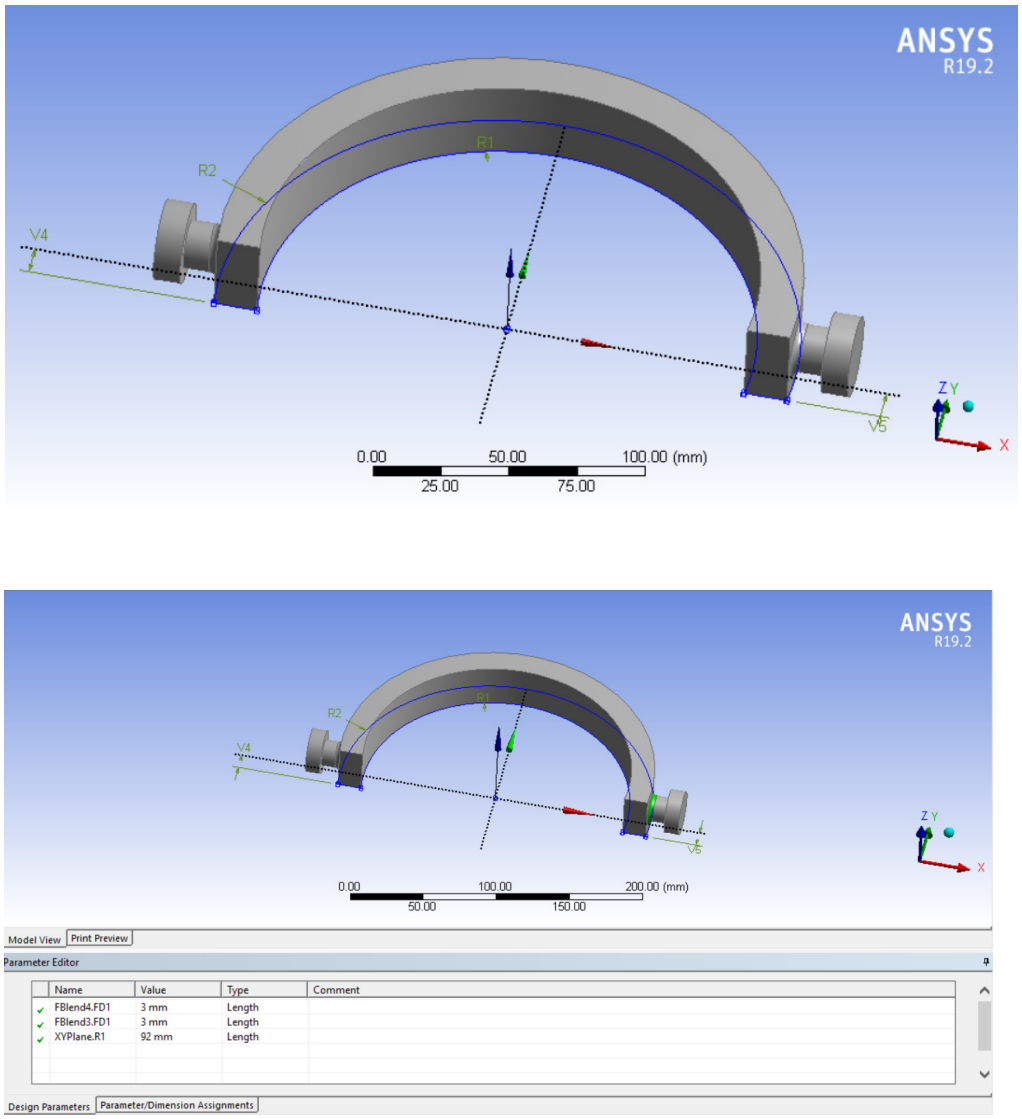

Figure 32. Parameters selected as input in the optimization process.

The output parameters are the guide mass as well as the von Mises equivalent stress. The initial guide mass is calculated based on the definition of the guide material and has a value of 0.54397 kg. The von Mises equivalent stress is calculated after running structural static analysis.

The worst-case loading condition of the circular guide is when the element that rests on the guide is in the extreme position, in which case the guide is subject to a compound stress of both twisting and bending. For finite element analysis, we specified the boundary conditions and loads according to the real model. Thus, we defined rotation Joints A and B between the circular guide and the casing. A torque of 5000 N mm acts on the drive end of the guide, while a fixed support is defined on the opposite end. For discretization of the guide into finite elements, we used hexahedral elements and specified a finite element size of 2 mm. The discretized structure comprises 130,489 elements and 31,668 nodes.

Figure 33 shows two important aspects for the construction of the finite element model, namely the definition of the torsional moment and the finite element discretization of the circular guide.

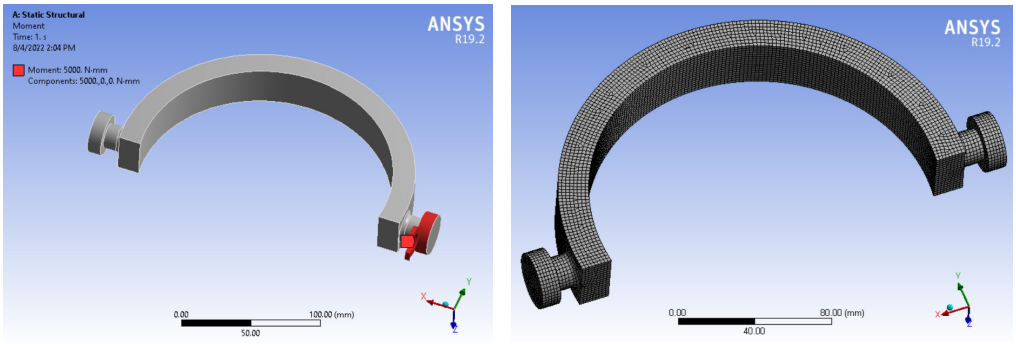

Figure 33. Definition of boundary conditions and discretization into finite elements.

4.2. Running Transient Structural Analysis

Thus, Figure 34 shows the distribution of the equivalent von Mises stresses, the maximum principal stresses, the distribution of the equivalent specific strains, and the total displacements.

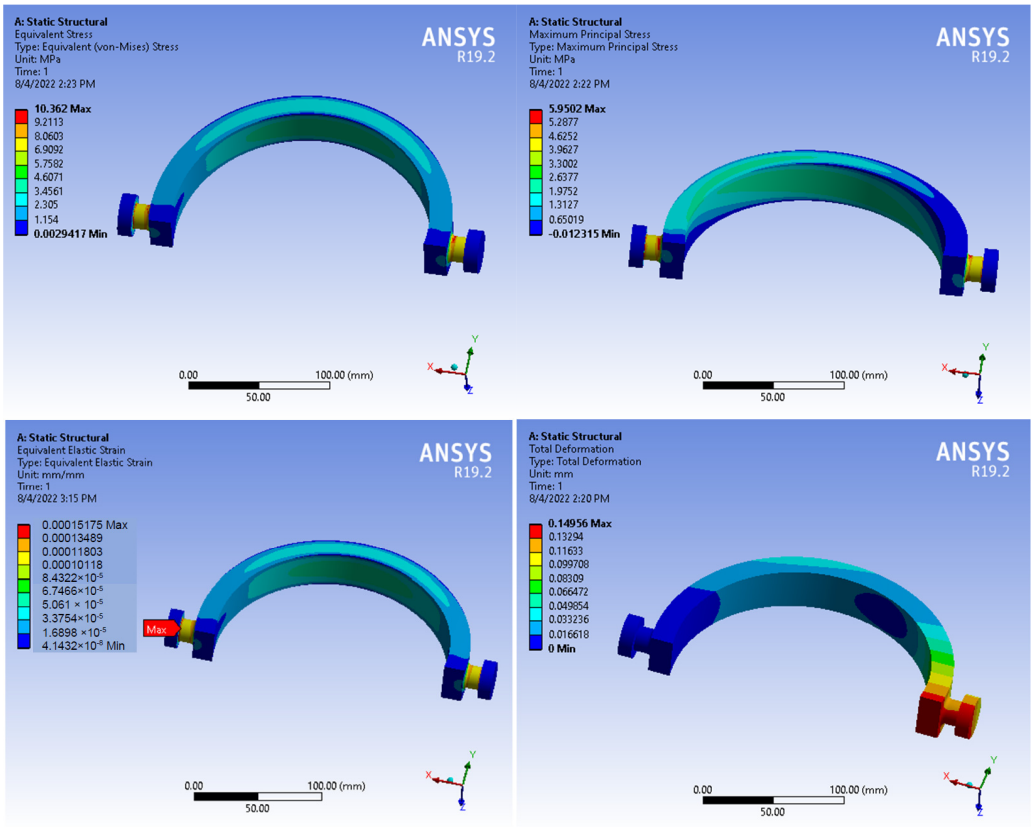

Figure 34. Results of mechanical stresses, displacements, and strains for non-optimized structure.

At this stage, the maximum von Mises equivalent stress of 10.362 MPa is defined as the output parameter.

4.3. Conduct a Design-of-Experiments Study

Based on a design-of-experiments (DE) study, central composite design, several possible design variants are calculated, as shown in Table 25. There are 15 possible design solutions of the considered structure. For each design point of the structure, we present on the line related to the respective DP the values of the input parameters (P1, P2-radii of

the connection (Blend), and P3-radius R1) and the output parameters (P4-Solid Mass and P5-Equivalent Stress Maximum). From these results, the following is found:

- For the output parameter P4-Solid Mass, the minimum calculated value is 0.27269 kg, and the maximum is 0.79132 kg;
- For the output parameter P5-Equivalent Stress, the minimum calculated value is 10.125 MPa, and the maximum is 19.837 MPa.

Table 25. Design points of design-of-experiments.

Param. / No.	Design Point	P1—FBlend4.FD1 (mm)	P2—FBlend3.FD1 (mm)	P3—XYPlane.R1 (mm)	P4—Solid Mass (kg)	P5—Equivalent Stress Maximum (MPa)
1	1 DP	3	3	92	0.54397	10.362
2	2	2.7	3	92	0.54391	10.159
3	3	3.3	3	92	0.54403	10.3
4	4	3	2.7	92	0.54391	10.125
5	5	3	3.3	92	0.54403	10.304
6	6	3	3	82.8	0.79132	10.205
7	7	3	3	101.2	0.27269	19.837
8	8	2.7561	2.7561	84.52	0.7468	10.415
9	9	3.2439	2.7561	84.52	0.7469	10.297
10	10	2.7561	3.2439	84.52	0.7469	10.302
11	11	3.2439	3.2439	84.52	0.74699	10.364
12	12	2.7551	2.7561	99.48	0.32514	13.127
13	13	3.2439	2.7561	99.48	0.32523	13.126
14	14	2.7561	3.2439	99.48	0.32523	13.131
15	15	3.2439	3.2439	99.48	0.32533	13.127

5. Obtaining a Response Surface

A response surface is a 2D or 3D graph showing the variation of output parameters relative to an input parameter. Table 26 shows the results of a Min–Max Search analysis. The table shows the minimum (lines 3 and 4) and maximum (lines 6 and 7) values of the output parameters P4 and P5. Obviously, increasing the input parameter P1 causes a decrease in output parameter P4 (Mass) and an increase in parameter P5 (Equivalent Stress).

Table 26. Min–Max Search.

Name	P1—FBlend4.FD1 (mm)	P2—FBlend3.FD1 (mm)	P3—XYPlane.R1 (mm)	P4—Solid Mass (kg)	P5—Equivalent Stress Maximum (MPa)
Output Parameter Minimums					
P4-Solid Mass	2.7	2.7	101.2	**0.27258**	19.837
P5—Equivalent Stress Maximum	3.033	3.2561	89.656	0.60933	**10.211**
Output Parameter Maximums					
P4—Solid Mass	3.3	3.3	82.8	**0.79144**	10.351
P5—Equivalent Stress Maximum	3.183	2.7264	101.2	0.27268	**19.837**

The response surfaces obtained are shown in Figures 35 and 36. Calculation of response surfaces is necessary because the next step is to optimize these surfaces in order to obtain an optimal solution.

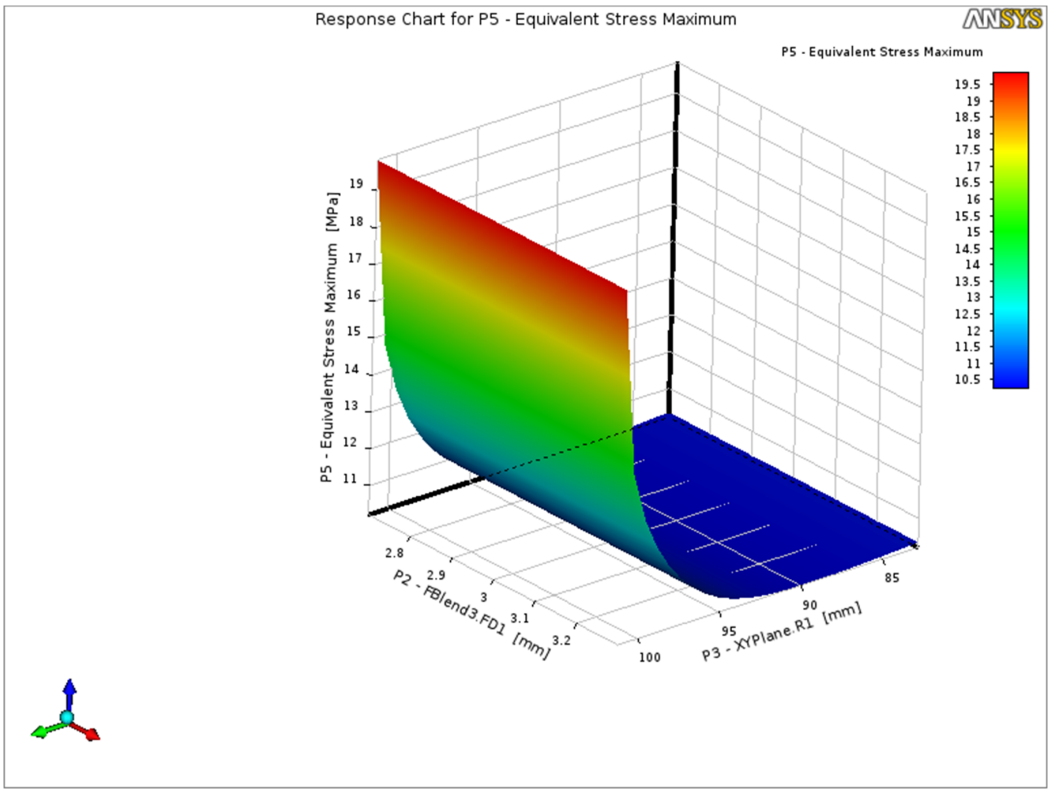

Figure 35. Response chart for P6—Equivalent Stress Maximum vs. P1 and P3.

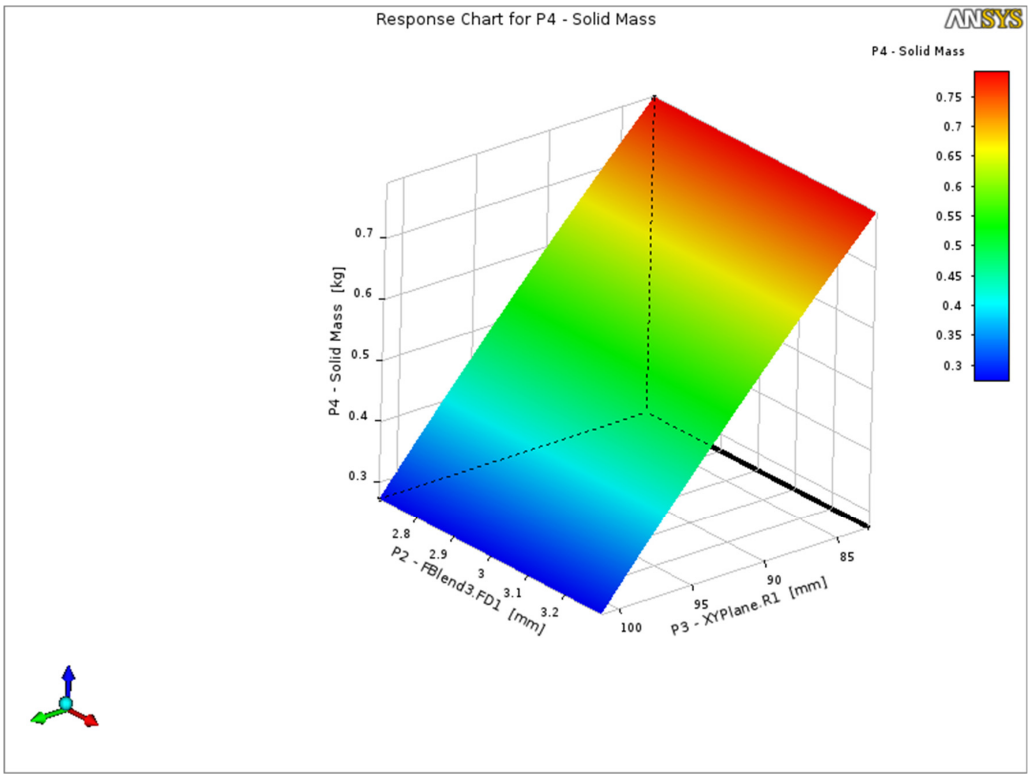

Figure 36. Response chart for P4—Solid Mass vs. P1 and P3.

The computed response surface design parameters (Solid Mass and Equivalent Stress Maximum) characteristics are shown in the Table 27.

Table 27. Response surface parameters.

Characteristic \ Parameter	P4—Solid Mass	P5—Equivalent Stress Maximum
Coefficient of Determination (Best Value = 1)		
Learning Points	★★★ 1	★★★ 0.99915
Cross-Validation on Learning Points	★★★ 1	★★★ 0.99857
Root Mean Square Error (Best Value = 0)		
Learning Points	3.32288×10^{-7}	0.073305
Cross-Validation on Learning Points	7.1713×10^{-7}	0.094999
Relative Maximum Absolute Error (Best Value = 0%)		
Learning Points	★★★ 0	5.6275
Cross-Validation on Learning Points	★★★ 0.0010358	7.434
Relative Average Absolute Error (Best Value = 0%)		
Learning Points	★★★ 0	★★ 1.954
Cross-Validation on Learning Points	★★★ 0.00029053	★ 2.7089

★ —not acceptable; ★★ —acceptable; ★★★ —excellent.

Response Surface Optimization

Optimization involves minimizing the output parameter P5, maximum equivalent von Mises stress, and minimizing parameter P4, mass. The defined optimization constraint assumes that the equivalent von Mises stress does not exceed 14 MPa.

Table 28 shows the purpose of the optimization, i.e., the minimization of the input parameters P4 and P5, specifies the optimization method used, and details the 3 points of the optimization surface that are candidates for the optimal solution.

Table 28. Optimization study.

Optimization Study			
Minimize P5; P5 $\leq$ 14 MPa	Goal, Minimize P5 (Default importance); Strict constraint, P5 values less than or equal cu 14 MPa (Default importance)		
Minimize P4	Goal, Minimize P4 (Default importance)		
Optimization Method			
MOGA	The MOGA method (Multi-Objective Genetic Algorithm) is a variant of the popular NSGA-II (Non-dominated Sorted genetic Algorithm-II) based on controlled elitism concept. It supports multiple objectives and constraints and aims at finding the global optimum.		
Configuration	Generate 300 samples initially, 600 samples per iteration and find 3 candidates in a maximum of 20 iterations.		
Status	Converged after 3509 evaluations.		
Candidate Points			
	Candidate Point 1	**Candidate Point 2**	**Candidate Point 3**
P1—FBlend4. FD1 (mm)	2.8361	3.0327	3.0587
P2—FBlend3. FD2 (mm)	2.7499	3.2963	3.0008
P3—XYPlane.R1 (mm)	97.543	98.151	95.869
P4—Solid Mass (kg)	★★ 0.3833	★★ 0.36531	★ 0.43281
P5—Equivalent Stress Maximum (MPa)	★★ 11.539	★★ 11.919	★★ 10.834

★ —not acceptable; ★★ —acceptable.

Table 29 shows the results obtained for the three design solutions (candidate points). Candidate Point 2 is identified as the optimal solution, for which the values of the input parameters are: P1 = 3.0327 mm, P2 = 3.2963 mm, and P3 = 98.151 mm, and the values obtained for the output parameters are: P4 = 0.36531 mm and P5 = 11.919 MPa.

Table 29. Optimization candidate points.

Name	P1—FBlend4.FD1 (mm)	P2—FBlend3.FD1 (mm)	P3—XYPlane.R1 (mm)	P4—Solid Mass (kg)		P5—Equivalent Stress Maximum (MPa)	
				Parameter Value	Variation from Reference	Parameter Value	Variation from Reference
Candidate Point 1	2.8361	2.7499	97.543	★★ 0.3833	4.92%	★★ 11.539	−3.18%
Candidate Point 2	3.0327	3.2963	98.151	★★ 0.36531	0.00%	★★ 11.919	0.00%
Candidate Point 3	3.0587	3.0008	95.869	★ 0.43281	18.48%	★★ 10.834	−9.10%

★ —not acceptable; ★★ —acceptable.

The goal of structural optimization is to achieve more-uniform distribution of stresses and strains to eliminate stress concentrators, to increase fatigue strength, and, most importantly, to reduce the mass of the guide.

As shown in Figure 37 this objective has been achieved. Symmetrical stress distribution is observed, and the optimization constraint of keeping the maximum stresses below the imposed limit is fulfilled.

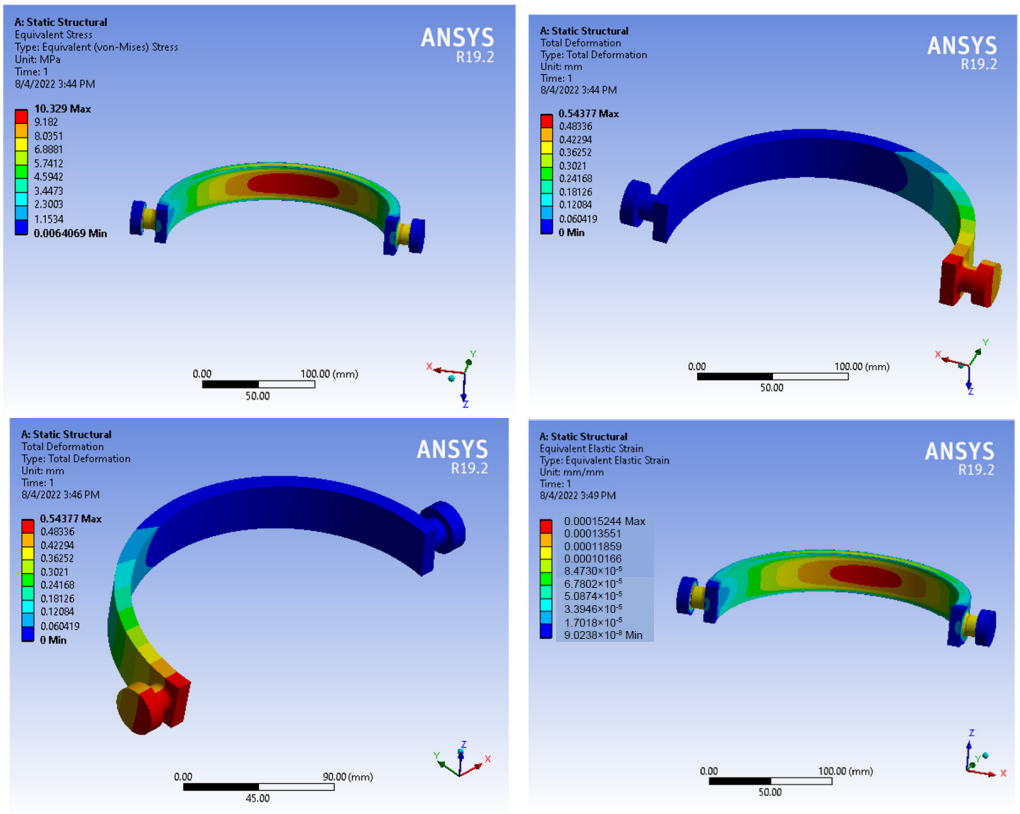

Figure 37. Results of mechanical stresses, displacements, and deformations for the optimized structure.

6. Experimental Determination of the Robot Module Actuation Torques

The robotic system is tested in laboratory conditions using a healthy subject (with informed consent). The tested subject is 1.85 m height and weighs 88 kg, which leads to

hand weight (according to [51]) similar to the simulation loads presented in Figure 21. The results are shown in Figure 38, which presents the time history diagram of the torque required for the flexion–extension motion for seven cycles with the following motion parameters: motion amplitude (range of motion) of 60° (both for flexion and extension) and speed of 30°/s. The torque is estimated using the MC_ReadActualTorque (FB) function in Automation Studio, B & R Automation [47], which provides an approximate value of the required motor torque. The maximum required value of the torque is 4.5 Nm, while the average is 0.0821 Nm. Figure 39 presents the time history diagram of the radial–ulnar deviation motion for seven cycles using the following motion parameters: radial motion amplitude of 20°, ulnar motion amplitude of 30° and speed of 30°/s. The maximum required torque value is −26 Nm, while the average is −10.887 Nm.

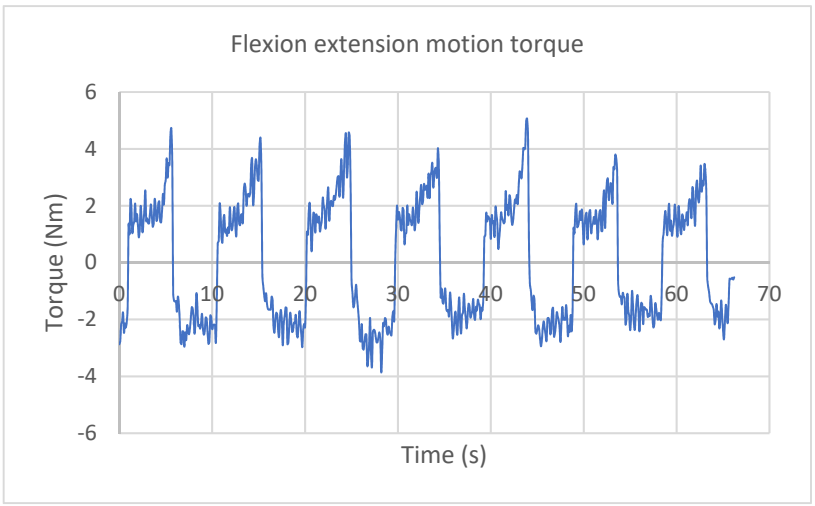

Figure 38. The time history diagram for the flexion–extension motion of the ParReEx-wrist robotic system.

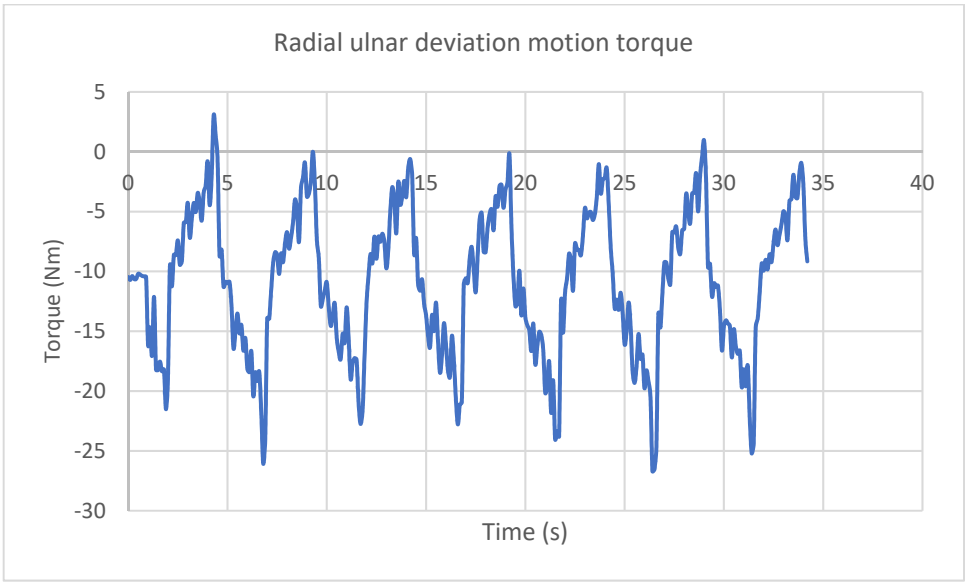

Figure 39. The time history diagram for the radial–ulnar deviation motion of the ParReEx-wrist robotic system.

Very good agreement is observed between the smoothness of the actuation moments determined by numerical simulation and experimentally, as shown in Figures 21, 38 and 39. This validates the results obtained by numerical simulation in ADAMS.

7. Discussion

Simulations of ParReEx robot dynamics were performed in three simulation cases: (1) without friction in the couplings, (2) with friction, and (3) with friction and flexible elements.

The evolution of the RMS value of the resulting connecting forces in Couplings A and B for the three simulation scenarios is shown in Figure 40. The RMS value of a set of values (or a continuous-time waveform) is the square root of the arithmetic mean of the squares of the values, or the square of the function that defines the continuous waveform.

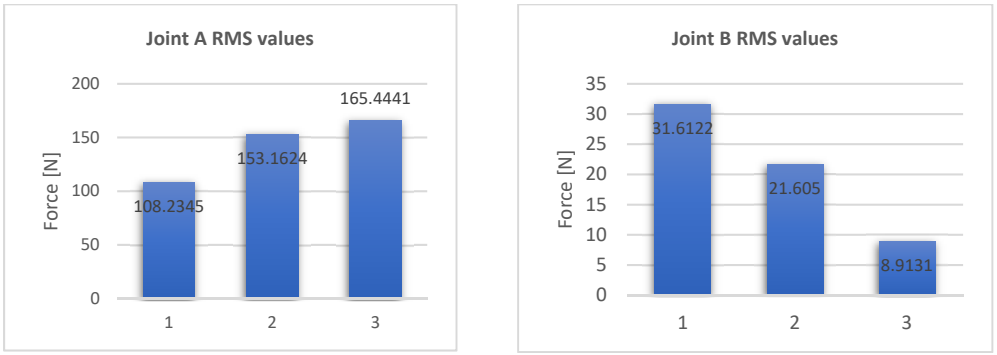

Figure 40. Evolution of the RMS values for the connection forces in Couplings A and B.

The presence of friction in the coupling increases the reaction in Coupling A and decreases the reaction in Coupling B. This can be explained by the fact that charging Coupling A unloads Coupling B. The presence of a toothed belt drive in Coupling A causes additional loading of this driving joint. In this case, the bearing in Coupling B will be a driving one, i.e., it will also take up the axial forces that occur in the circular guide element.

For the other couplings, friction increases the RMS values of the resulting connecting forces. Thus, Figure 41 shows the evolution of the RMS values for the resultant coupling forces in R1 and R2.

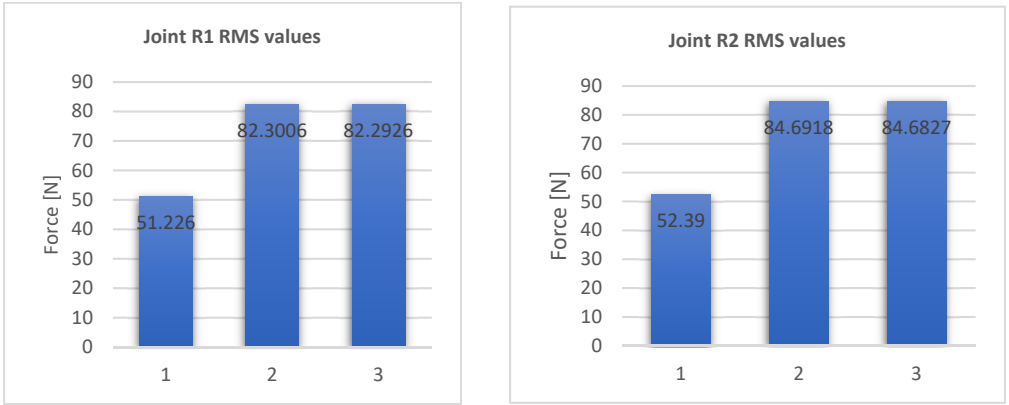

Figure 41. Evolution of the RMS values for the connection forces in Joints R1 and R2.

Further, friction increased the actuation moment for flexion–extension (Torque 1) and radial–ulnar deviation (Torque 2), as Figure 42 illustrates.

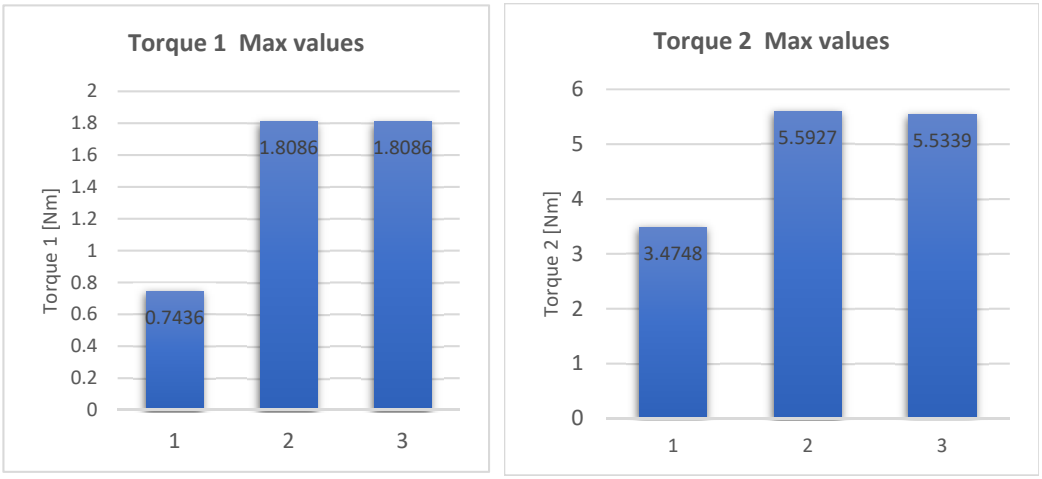

Figure 42. Evolution of the maximum values for the moments of actuation for flexion–extension and radial–ulnar deviation motions.

Numerical simulation in ADAMS (Figure 21) showed that flexion–extension motion of the wrist joint required a maximum moment of 1.8086 Nm, and radial–ulnar deviation required a maximum moment of 5.5339 Nm. Experimentally, higher values were obtained for these parameters: 4.5 Nm for flexion–extension and 20 Nm for radial–ulnar deviation. As a remark on the experimentally determined values, it is found that these quantities do not start from zero, so in the initial starting position, the system is preloaded by the human subject's arm. The same happened in the numerical simulation in ADAMS, only in the simulation we considered the load produced by the patient's arm of 30 N as a constant load.

We also found that the experimentally measured values for the actuation moments have similar variation. The differences between the experimentally measured values and those obtained by numerical simulation can be explained as follows:

✓ In the case of numerical simulation, we defined the motion law by the STEP function, and at the end of the stroke the angular velocity is reduced, which is not the case in the experimental case;

✓ The virtual prototype does not consider the presence of clearance in the kinematic joints. In the case of the experimental prototype, these clearances are inherent, so the components could not be assembled. The presence of these clearances produces jumps of moments at the end of the stroke, which is not the case with the virtual simulation.

8. Conclusions

In this paper, we conducted a study on the dynamics of the ParReEx robot used for the wrist joint. Dynamic analysis was performed using MSC.ADAMS in three simulation scenarios:

(a) Kinematic elements were considered rigid bodies and friction in the kinematic couplings was not considered;

(b) Kinematic elements were considered rigid bodies and friction in the robot couplings was considered;

(c) Both flexibility of kinematic elements and friction in the couplings were considered.

Structural optimization of the circular guide of the ParReEx robot using ANSYS software was performed.

The differences between the experimentally measured values and those obtained by numerical simulation are acceptable for the following reasons:

- Parts made by 3D printing have tolerances within 0.2 mm. For this reason, the experimental model is in real assembly conditions;
- Similar variations of torsional moments were determined experimentally and by numerical simulation in ADAMS, which validates the two models.

Dynamic analysis allows us to draw conclusions about the operational safety of a robotic system. A next step is dynamic optimization of the robotic structure. Structural optimization can eliminate stress concentrators in the robot structure, which contributes to increased operational safety.

The results obtained by numerical simulation were validated by experimental measurements. Thus, the actuation moments for the two movements of the wrist joint—flexion–extension and radial–ulnar deviation—were determined experimentally. Concordance between the variations determined by numerical simulation and those determined experimentally was observed.

Author Contributions: Conceptualization, D.T., I.D.G., D.P. and G.C.; methodology, D.T., I.D.G. and D.P.; software, I.D.G. and D.T.; validation, P.T., B.G., N.T., C.A. and D.N.T.; formal analysis, I.D.G., P.T. and B.G.; investigation, I.D.G., D.T. and D.P.; resources, D.T.; writing—original draft preparation, I.D.G. and D.T.; writing—review and editing, D.P., B.G. and G.C.; visualization, D.N.T., N.T. and C.A.; supervision, D.T., D.P. and G.C.; project administration, D.P. All authors have read and agreed to the published version of the manuscript.

Funding: This work was supported by a grant from the Romanian Ministry of Research and Innovation, CCCDI—UEFISCDI, project number PN-III-P2-2.1-PED-2019-3022/546PED/2020 (NeuroAssist) within PNCDI III, and by the project POCU/380/6/13/123927—ANTREDOC, "Entrepreneurial competencies and excellence research in doctoral and postdoctoral studies programs", co-funded from the European Social Fund through the Human Capital Operational Program 2014–2020.

Institutional Review Board Statement: Not applicable.

Informed Consent Statement: All subjects gave their informed consent for inclusion before they participated in the study. The study was conducted in accordance with the Declaration of Helsinki, and the protocol was approved by the Ethics Committee of NeuroAssist project.

Data Availability Statement: The data presented in this study are openly available in the reference number.

Conflicts of Interest: The authors declare no conflict of interest.

References

1. Klamroth-Marganska, V.; Blanco, J.; Campen, K.; Curt, A.; Dietz, V.; Ettlin, T.; Felder, M.; Fellinghauer, B.; Guidali, M.; Kollmar, A.; et al. Three-dimensional, task-specific robot therapy of the arm after stroke: A multicentre, parallel-group randomised trial. *Lancet Neurol.* **2014**, *13*, 159–166. [CrossRef]
2. Lindsay, M.P.; Norrving, B.; Sacco, R.L.; Brainin, M.; Hacke, W.; Martins, S.; Pandian, J.; Feigin, V. World stroke organization (WSO): Global stroke fact sheet 2019. *Int. J. Stroke* **2019**, *14*, 806–817. [CrossRef] [PubMed]
3. Feigin, V.L.; Norrving, B.; Mensah, G.A. Global Burden of Stroke. *Circ. Res.* **2017**, *120*, 439–448. [CrossRef] [PubMed]
4. Virani, S.S.; Alonso, A.; Benjamin, E.J.; Bittencourt, M.S.; Callway, C.W.; Carson, A.P.; Chamberlain, A.M.; Chang, A.R.; Cheng, S.; Delling, F.N.; et al. Heart disease and stroke statistics-2020 update: A report from the Americanheart association. *Circulation* **2020**, *141*, e1–e458. [CrossRef] [PubMed]
5. Skilbeck, C.E.; Wade, D.T.; Hewer, R.L.; Wood, V.A. Recovery after stroke. *J. Neurol. Neurosurg. Psychiatry* **1982**, *46*, 5–8. [CrossRef]
6. Kwakkel, G.; Kollen, B.J.; Van der Grond, J.; Prevo, A.J. Probability of regaining dexterity in the flaccid upper limb: Impact of severity of paresis and the time since onset in acute stroke. *Stroke* **2003**, *34*, 2181–2186. [CrossRef]
7. Sivan, M.; Gallagher, J.; Makower, S.; Keeling, D.; Bhakta, B.; O'Connor, R.J.; Levesley, M. Home-based computer assisted arm rehabilitation robotic device for upper limb exercise after stroke: Result of feasibility study in home setting. *J. Neuroeng. Rehabil.* **2014**, *11*, 163. [CrossRef]
8. Gorelick, P.B. The global burden of stroke: Persistent and disabling. *Lancet Neurol.* **2019**, *18*, 417–418. [CrossRef]
9. Murie-Fernandez, M.; Irimia, P.; Martinez-Vila, E.; Meyer, M.J.; Teasell, R. Neuro-rehabilitation after stroke. *Neurol.* **2010**, *25*, 189–196. [CrossRef]
10. Van Peppen, R.P.; Kwakkel, G.; Wood-Dauphinee, S.; Hendriks, H.J.; Van der Wees, P.J.; Dekker, J. The impact of physical therapy on functional outcomes after stroke: What's the evidence? *Clin. Rehabil.* **2004**, *18*, 833. [CrossRef]
11. Jarrassé, N.; Proietti, T.; Crocher, V.; Robertson, J.; Sahbani, A.; Morel, G.; Roby-Brami, A. Robotic exoskeletons: A perspective for the rehabilitation of arm coordination in stroke patients. *Front. Hum. Neurosci.* **2014**, *8*, 1845–1846. [CrossRef] [PubMed]
12. Yamamoto, I.; Inagawa, N.; Matsui, M.; Hachisuka, K.; Wada, F.; Hachisuka, A. Research and development of compact wrist rehabilitation robot system. *Bio-Med. Mater. Eng.* **2014**, *24*, 123–128. [CrossRef] [PubMed]
13. Loureiro, R.C.V.; Harwin, W.; Nagai, K.; Johnson, M. Advances in upper limb stroke rehabilitation: A technology push. *Med. Biol. Eng. Comput.* **2011**, *49*, 1103–1118. [CrossRef] [PubMed]

14. Volpe, B.T.; Huerta, P.T.; Zipse, J.L.; Rykman, A.; Edwards, D.; DiPietro, L.; Hogan, N.; Krebs, H.I. Robotic Devices as Therapeutic and Diagnostic Tools for Stroke Recovery. *Arch. Neurol.* **2009**, *66*, 1086–1090. [CrossRef]
15. Reinkensmeyer, D.J. Robotic Assistance for Upper Extremity Training after Stroke. In *Advanced Technologies in Rehabilitation*; Gaggioli, A., Keshner, E.A., Weiss, P.L., Riva, E., Eds.; IOS Press: Amsterdam, The Netherlands, 2009; pp. 25–39.
16. Huang, J.; Tu, X.; He, J. Design and evaluation of RUPERT wearable upper extremity exoskeleton robot for clinical and in home therapies. *IEEE Trans. Syst. Man Cybern. Syst.* **2016**, *46*, 926–935. [CrossRef]
17. Vaida, C.; Plitea, N.; Carbone, G.; Birlescu, I.; Ulinici, I.; Pisla, A.; Pisla, D. Innovative development of a spherical parallel robot for upper limb rehabilitation. *Int. J. Mech. Robot. Syst.* **2018**, *4*, 256–276. [CrossRef]
18. Pisla, D.; Tarnita, D.; Tucan, P.; Tohanean, N.; Vaida, C.; Geonea, I.D.; Bogdan, G.; Abrudan, C.; Carbone, G.; Plitea, N. A Parallel Robot with Torque Monitoring for Brachial Monoparesis Rehabilitation Tasks. *Appl. Sci.* **2021**, *11*, 9932. [CrossRef]
19. Geonea, I.D.; Tarnita, D.; Pisla, D.; Carbone, G.; Bolcu, A.; Tucan, P.; Georgescu, M.; Tarniță, D.N. Dynamic Analysis of a Spherical Parallel Robot Used for Brachial Monoparesis Rehabilitation. *Appl. Sci.* **2021**, *11*, 11849. [CrossRef]
20. Tarnita, D.; Marghitu, D. Analysis of a hand arm system. *Robot. Comput. Integr. Manuf.* **2013**, *29*, 493–501. [CrossRef]
21. Gull, M.A.; Bai, S.; Bak, T. A Review on Design of Upper Limb Exoskeletons. *Robotics* **2020**, *9*, 16. [CrossRef]
22. Veerbeek, J.M.; Langbroek-Amersfoort, A.C.; Van Wegen, E.E.; Meskers, C.G.; Kwakkel, G. Effects of robot-assisted therapy for the upper limb after stroke. *Neurorehabilit. Neural Repair* **2017**, *31*, 107–121. [CrossRef] [PubMed]
23. Zengin-Metli, D.; Özbudak-Demir, S.; Eraktaş, İ.; Binay-Safer, V.; Ekiz, T. Effects of robot assistive upper extremity rehabilitation on motor and cognitive recovery, the quality of life, and activities of daily living in stroke patients. *J. Back Musculoskelet. Rehabil.* **2018**, *31*, 1059–1064. [CrossRef] [PubMed]
24. Kim, G.; Lim, S.; Kim, H.; Lee, B.; Seo, S.; Cho, K.; Lee, W. Is robot-assisted therapy effective in upper extremity recovery in early stage stroke?—A systematic literature review. *J. Phys. Therapy Sci.* **2017**, *29*, 1108–1112. [CrossRef] [PubMed]
25. Shahar, N.; Schwartz, I.; Portnoy, S. Differences in muscle activity and fatigue of the upper limb between Task-Specific training and robot assisted training among individuals post stroke. *J. Biomech.* **2019**, *89*, 28–33. [CrossRef] [PubMed]
26. Bian, H.; Chen, Z.; Wang, H.; Zhao, T. Mechanical design of EFW Exo II: A hybrid exoskeleton for elbow-forearm-wrist rehabilitation. In Proceedings of the 2017 International Conference on Rehabilitation Robotics (ICORR), London, UK, 17–20 July 2017; pp. 689–694. [CrossRef]
27. Geonea, I.D.; Tarnita, D. Design and evaluation of a new exoskeleton for gait rehabilitation. *Mech. Sci.* **2017**, *8*, 307–321. [CrossRef]
28. Tarnita, D.; Geonea, I.; Petcu, A.; Tarnita, D.N. Numerical simulations and experimental human gait analysis using wearable sensors. In *International Workshop on Medical and Service Robots*; Springer: Cham, Switzerland, 2016; pp. 289–304.
29. Berceanu, C.; Tarnita, D.; Filip, D. About an experimental approach used to determine the kinematics of the human movement. *J. Solid State Phenom. Robot. Autom. Syst.* **2010**, *166–167*, 45–50. [CrossRef]
30. Tarnita, D.; Pisla, D.; Geonea, I.; Vaida, C.; Catana, M.; Tarnita, D.N. Static and Dynamic Analysis of Osteoarthritic and Orthotic Human Knee. *J. Bionic Eng.* **2019**, *16*, 514–525. [CrossRef]
31. Tarnita, D.; Catana, M.; Dumitru, N.; Tarnita, D.N. Design and simulation of an orthotic device for patients with osteoarthritis. In *New Trends in Medical and Service Robots*; Springer: Cham, Switzerland, 2016; pp. 61–77.
32. Hussain, S.; Jamwal, P.K.; Van Vliet, P.; Ghayesh, M.H. State-of-the-Art Robotic Devices for Wrist Rehabilitation: Design and Control Aspects. *IEEE Trans. Hum. Mach. Syst.* **2020**, *50*, 361–372. [CrossRef]
33. Krebs, H.I.; Volpe, B.T.; Williams, D.; Celestino, J.; Charles, S.K.; Lynch, D.; Hogan, N. Robot-Aided Neurorehabilitation: A robot for wrist rehabilitation. *IEEE Trans. Neural Syst. Rehabil. Eng.* **2007**, *15*, 327. [CrossRef]
34. Hogan, N.; Krebs, H.I.; Charnnarong, J.; Srikrishna, P.; Sharon, A. MIT-MANUS: A workstation for manual therapy and training II. In *Proceedings IEEE International Workshop on Robot and Human Communication*; IEEE: New York, NY, USA, 1992; Volume 1833, pp. 161–165.
35. Krebs, H.I.; Celestino, J.; Williams, D.; Ferraro, M.; Volpe, B.; Hogan, N. A Wrist extension for MIT-MANUS. *Adv. Rehabil. Robot.* **2004**, *306*, 377–390.
36. Cappello, L.; Elangovan, N.; Contu, S.; Khosravani, S.; Konczak, J.; Masia, L.; Konczak, J. Robot-aided assessment of wrist proprioception. *Front. Hum. Neurosci.* **2015**, *9*, 198. [CrossRef] [PubMed]
37. Pehlivan, A.U.; Sergi, F.; Erwin, A.; Yozbatiran, N.; Francisco, G.E.; O'Malley, M.K. Design and validation of the RiceWrist-S exoskeleton for robotic rehabilitation after incomplete spinal cord injury. *Robotica* **2014**, *32*, 1415–1431. [CrossRef]
38. Amirabdollahian, F.; Ates, S.; Basteris, A.; Cesario, A.; Buurke, J.; Hermens, H.; Hofs, D.; Johansson, E.; Mountain, G.; Nasr, N.; et al. Design, development and deployment of a hand/wrist exoskeleton for home-based rehabilitation after stroke—SCRIPT project. *Robotica* **2014**, *32*, 1331–1346. [CrossRef]
39. Yin, L.; Huang, L.; Huang, J.; Tian, L.; Li, F. Solution-region-based synthesis approach for selecting optimal four-bar linkages with the Ball–Burmester point. *Mech. Sci.* **2019**, *10*, 25–33. [CrossRef]
40. Saadatzi, M.; Long, D.C.; Celik, O. Comparison of human–robot interaction torque estimation methods in a wrist rehabilitation exoskeleton. *J. Intell. Robot. Syst.* **2018**, *94*, 565–581. [CrossRef]
41. Bae, S.J.; Jang, S.H.; Seo, J.P.; Chang, P.H. The optimal speed for cortical activation of passive wrist movements performed by a rehabilitation robot: A functional NIRS study. *Front. Hum. Neurosci.* **2017**, *11*, 194. [CrossRef]
42. Zhang, L.; Li, J.; Cui, Y.; Dong, M.; Fang, B.; Zhang, P. Design and performance analysis of a parallel wrist rehabilitation robot (PWRR). *Robot. Auton. Syst.* **2020**, *125*, 103390. [CrossRef]

43. Carbone, G.; Gherman, B.; Ulinici, I.; Vaida, C.; Pisla, D. Design issues for an inherently safe robotic rehabilitation device. *Mech. Mach. Sci.* **2018**, *49*, 1025–1032.
44. Bhattacharya, S.; Nenchev, D.N.; Uchiyama, M. A recursive formula for the inverse of the inertia matrix of a parallel manipulator. *J. Mech. Mach. Theory* **1998**, *33*, 957–964. [CrossRef]
45. Codourey, A.; Burdet, E. A body oriented method for finding a linear form of the dynamic equatiojns of fully parallel robot. In Proceedings of the International Conference on Robotics and Automation, Albuquerque, NM, USA, 25 April 1997; pp. 1612–1619.
46. Dasgupta, B.; Mruthyunjaya, T.S. Closed-form dynamic equations of the general Stewart platform through the Newton–Euler approach. *J. Mech. Mach. Theory* **1998**, *33*, 993–1012. [CrossRef]
47. Tucan, P.; Gherman, B.; Major, K.; Vaida, C.; Major, Z.; Plitea, N.; Carbone, G.; Pisla, D. Fuzzy Logic-Based Risk Assessment of a Parallel Robot for Elbow and Wrist Rehabilitation. *Int. J. Environ. Res. Public Health* **2020**, *17*, 654. [CrossRef]
48. Tarnita, D.; Geonea, I.; Petcu, A.; Tarnita, D.-N. Experimental Characterization of Human Walking on Stairs Applied to Humanoid Dynamics. *Adv. Robot. Des. Intell. Control.* **2017**, *540*, 293–301.
49. Gherman, B.; Pisla, D.; Plitea, N.; Vaida, C.; Carbone, G.; Pisla, A.; Banica, A. Parallel Robotic System for Upper Limb Medical Recovery. Patent Number OSIM: 132,234, 14 June 2017.
50. Pennestri, E.; Rossi, V.; Salvini, P.; Valentini, P.P. Review and Comparison of Dry Friction Force Models. *Nonlinear Dyn.* **2016**, *83*, 1785–1801. [CrossRef]
51. Contini, R.; Drillis, R.J.; Bluestein, M. Determination of Body Segment Parameters. *Hum. Factors* **1963**, *5*, 493–504. [CrossRef] [PubMed]